

**SWITCHABLE PARALLEL ELASTIC ACTUATORS
IN MONOPOD AND QUADRUPED APPLICATIONS**

by

Anthony Rossi

A thesis submitted to the Faculty of the University of Delaware in partial fulfillment of the requirements for the degree of Master of Science in Mechanical Engineering

Winter 2019

© 2019 Anthony Rossi
All Rights Reserved

**SWITCHABLE PARALLEL ELASTIC ACTUATORS
IN MONOPOD AND QUADRUPED APPLICATIONS**

by

Anthony Rossi

Approved: _____
Ioannis, Poulakakis, Ph.D.
Professor in charge of thesis on behalf of the Advisory Committee

Approved: _____
Ajay Prasad, Ph.D.
Chair of the Department of Mechanical Engineering

Approved: _____
Levi Thompson, Ph.D.
Dean of the College of Engineering

Approved: _____
Douglas J. Doren, Ph.D.
Interim Vice Provost for Graduate and Professional Education

ACKNOWLEDGMENTS

First, I would like to thank Dr. Poulakakis for his guidance and support throughout this journey; without it, none of this would have been possible. His help and insight not only extends throughout my graduate school tenure, but also dates back to my undergraduate time, both as a student and undergraduate research assistant in his lab. The time spent working with him on the multiple research projects in the lab had not only taught me the technical knowledge relating robotics and control, but also the important skills around project and time management. His perseverance to create quality work has instilled in me a drive to continually push boundaries of success, and always strive for perfection.

Over the years, I was lucky to have a wonderful cohort of colleagues over the years who have not only been there to help with robotics challenges, but also have become close friends. Xin Liu, Qu Cao, Jian Huang, and Mohammad Shaflee were among the first students I met in the early days of the lab. Throughout the years Sushant Veer, Adam Stager, Rohit Kakodkar, Nathan Gigueré, Kevin Eckenhoff, and Duanyi Wei had created unforgettable memories, as well as an excellent atmosphere to work in. Additionally, I would like to thank Austin Crouse, Matt Schmittle, and Chris McMahon, for their time and help in both the mechanical hardware and electronics for SPEAR-II.

Lastly, I am thankful to my very loving and supportive parents Mary and Tony, and sister Kristen. I would like to thank Mikaila Ryan for her continual love and support throughout these many years in graduate school, and helping me stay balanced during the most difficult times of this journey.

TABLE OF CONTENTS

| | |
|--|-------------|
| LIST OF TABLES | vii |
| LIST OF FIGURES | viii |
| ABSTRACT | xii |
| Chapter | |
| 1 INTRODUCTION | 1 |
| 1.1 Motivation | 1 |
| 1.2 Literature Review | 2 |
| 1.2.1 Summary of Contributions | 6 |
| 1.3 Organization of the Thesis | 6 |
| 2 SPEAR-II: SECOND ITERATION OF SPEAR | 8 |
| 2.1 Concept of Sw-PEA | 8 |
| 2.2 Sw-PEA in a Monopod Setting | 8 |
| 2.3 SPEAR: First Iteration | 11 |
| 2.4 SPEAR-II: Second Iteration | 14 |
| 2.4.1 Knee Motor Change | 16 |
| 2.4.2 Mass and Inertia Reduction | 18 |
| 2.4.3 Toe and Foot Redesign | 20 |
| 2.4.4 Redesigned Boom | 23 |
| 2.4.5 Electronics Configuration Details | 25 |
| 2.5 Summary of SPEAR-II Design | 28 |
| 3 MODEL OF SPEAR-II | 30 |
| 3.1 Mechanical Model of System | 30 |

| | | |
|----------|--|-----------|
| 3.2 | Derivation of Dynamics | 33 |
| 3.3 | Dynamics in Floating-base Form | 36 |
| 4 | ANALYSIS AND EVALUATION OF SPEAR-II | 38 |
| 4.1 | Parameter Identification Experiments | 38 |
| 4.1.1 | Motivation | 38 |
| 4.1.2 | Experiment Model | 41 |
| 4.1.3 | Procedure of Experiment | 42 |
| 4.1.4 | Results and Analysis | 45 |
| 4.1.5 | Discussion and Summary | 48 |
| 4.1.5.1 | Increased Stiffness and Friction with Motor | 48 |
| 4.1.5.2 | Gearbox Effect on Dynamics | 49 |
| 4.1.5.3 | Negligible Electromechanical Interactions | 52 |
| 4.2 | Controller Tuning and Simulation | 57 |
| 4.2.1 | Controller for Hopping-in-Place | 57 |
| 4.2.2 | Simulation and Tuning of Control Parameters | 58 |
| 4.3 | Hopping Experiments with SPEAR-II | 60 |
| 5 | MODELING SPEAR-II AS A LEGGED TEMPLATE IN A QUADRUPEDAL SETTING | 65 |
| 5.1 | Model Overview | 66 |
| 5.2 | Controller | 70 |
| 5.2.1 | Stance Control | 71 |
| 5.2.2 | Swing Leg Control | 72 |
| 5.2.3 | Flight Phase Controller | 74 |
| 5.2.4 | Discrete-time Control Laws | 75 |
| 5.3 | Analysis of Results | 75 |
| 5.4 | Considerations for Quadruped Design | 78 |
| 6 | CONCLUSIONS AND FUTURE WORK | 82 |
| 6.1 | Conclusions | 82 |

| | | |
|-------|--|-----------|
| 6.2 | Future Work | 83 |
| 6.2.1 | Design of QSPEAR Quadruped | 83 |
| 6.2.2 | Regenerative Braking and Backdriving Experiments | 84 |
| 6.2.3 | Effects of Monopod Boom | 85 |
| 6.2.4 | Biped using SPEAR-II | 85 |
| | BIBLIOGRAPHY | 87 |
| | Appendix | |
| | COPYRIGHT PERMISSIONS | 92 |

LIST OF TABLES

| | | |
|-----|--|----|
| 2.1 | Overview of the design improvement goals for SPEAR-II. | 14 |
| 2.2 | Table showing the relevant design parameters and values for SPEAR-I. These parameters are used for assessment of the redesign effort in creating SPEAR-II. | 16 |
| 2.3 | Table highlighting the desired design specifications, SPEAR-II improvements, and tradeoffs (drawbacks) due to design decisions that were made. | 28 |
| 2.4 | Tabulation of significant parameters for the SPEAR-II leg. | 29 |
| 3.1 | Tabulation of Dynamics Parameters | 34 |
| 4.1 | Tabulation of the estimated model parameters using MATLAB [®] System Identification Toolbox. | 46 |
| 4.2 | Tabulation of the average estimated model parameters using MATLAB [®] System Identification Toolbox. | 46 |
| 5.1 | Tabulation of relevant parameters for the quadruped using SPEAR-II legs. | 70 |

LIST OF FIGURES

| | | |
|-----|---|----|
| 2.1 | Schematic of Sw-PEA mechanism design. Switching the key by engaging/disengaging into the chain, changes the stiffness at the joint from K1 to K2. Shown in [25] | 9 |
| 2.2 | Left: CAD model of Sw-PEA mechanism at the monopod foot. Right: Photo of SPEAR foot to implement the Sw-PEA at the knee joint of the robot. Note that the spring S_3 is a small spring with negligible stiffness, and is used to prevent binding with the key and chain. Shown in [26]. | 10 |
| 2.3 | Image of SPEAR-I leg depicting the various components of the Sw-PEA mechanism introduced into the leg design; see [26]. | 11 |
| 2.4 | Log-Log plot showing the cost of transport (COT) vs body mass of various robots and animals. The values for SPEAR-I are plotted to show comparison with other robots and animals; see [27]. | 12 |
| 2.5 | 3D CAD renderings of a conceptual quadrupedal robot using the SPEAR-I legs in the design. | 13 |
| 2.6 | Left: 3D CAD Model Rendering of the SPEAR-II design with slider boom. Right: Photo of SPEAR-II robot in stance phase. | 14 |
| 2.7 | Left: Photo of the first iteration of SPEAR; see [27]. Right: Photo of the second iteration of SPEAR (SPEAR-II) | 15 |
| 2.8 | The figure is a screenshot of the 3D CAD model of SPEAR-II to illustrate the geometric differences of the the newly implemented Maxon [®] motor (green coloring), and the previously used Faulhaber motor (blue coloring). | 17 |
| 2.9 | Diagrams of the locations of the thigh COM both SPEAR-I (left), and SPEAR-II (right). Notice the effect of improved dynamic balancing by relocating the knee motor to be above the hip axis. . . | 18 |

| | | |
|------|--|----|
| 2.10 | Photo focused on the timing pulley torque transmission mechanisms for SPEAR-II. | 19 |
| 2.11 | 3D CAD Model Rendering of the Foot Assembly on SPEAR-II. . . | 21 |
| 2.12 | Photo of a previous method of mounting the leg to the boom, illustrating the issue of a reaction moment due to the distance offset, d | 25 |
| 2.13 | Diagram showing the electronics on-board SPEAR-II. Note that while only one motor drive shows communication with the PC-104 stack, both have an identical connection with the CPU in practice (the arrows are not shown to reduce visual noise). | 26 |
| 3.1 | Side by side comparison of SPEAR-II with an abstracted model of the important forces at play during the stance phase. | 31 |
| 3.2 | Model of SPEAR-II in both stance and flight phase. | 33 |
| 4.1 | Energy flow diagram of SPEAR-I; see [27] | 40 |
| 4.2 | Model of the SPEAR-II leg in stance phase and the side view of the leg to compare during a parameter identification experiment. | 41 |
| 4.3 | Schematic of the SPEAR-II Leg during the push experiment. | 43 |
| 4.4 | The 6 different sets of experiments. Figures (a), (c), and (e) are all done with the motor engaged at the knee joint. Figures (b), (d), and (f) are conducted with the motor disengaged from the knee joint. | 47 |
| 4.5 | Plots comparing the model with experimental data, and simulation of corresponding models. | 49 |
| 4.6 | Simulation of the 10cm experiment varying gear ratios for SPEAR-II. | 51 |
| 4.7 | Experimental results illustrating the effect of the PWM amplifiers H bridge allowing the motor to rotate without additional resistance, as a no-load generator. | 53 |
| 4.8 | Simple circuit diagram of a basic H Bridge setup used in a conceptual motor control application. By changing the switches, the flow of current can control the direction of the motor, as well as braking and coasting. | 55 |

| | | |
|------|---|----|
| 4.9 | Model of the H bridge circuit used in the PWM amplifier for the Maxon (knee) motor in SPEAR-II. The structure is similar to the simple H bridge example shown in Fig. 4.8 but is expanded for the capability of handling the 3 motor phases of the brushless DC (BLDC) Motor. | 56 |
| 4.10 | Simulation results showing the knee angle of SPEAR-II during hopping-in-place gait. Note that the PD control during flight ensures that the knee angle reaches the desired touchdown angle before touchdown. | 60 |
| 4.11 | Joint angles of the Knee and Hip during hopping experiments: (a) Hip joint angle and (b) Knee joint angle | 61 |
| 4.12 | Measure and Reference Currents during hopping experiments. (a) Shows the knee current for both referenced (in red), and measured (in blue). (b) Shows the same plot for the hip current values for both referenced and measured. | 62 |
| 4.13 | Height of the boom during an 11-hop duration experiment. Note that despite the variations of the apex height of the boom, the controller is able to respond robustly and continue the hopping gait. | 63 |
| 5.1 | Photorealistic rendering of a 3D CAD model of a proposed quadruped using the SPEAR-II leg design. | 65 |
| 5.2 | Diagram displaying the footprint during the bounding gait cycle for a quadruped. | 67 |
| 5.3 | Model diagram of a quadrupedal robot using the SPEAR-II model (Q-SPEAR) as a legged platform. | 67 |
| 5.4 | Conceptual figure of the bounding cycle for a quadrupedal robot. | 68 |
| 5.5 | Plots showing the commanded knee torques from the motors for both the front (a) and back (b) legs throughout the simulation. | 77 |
| 5.6 | Plot showing the required knee torque for a variety of spring stiffness versus time. | 78 |
| 5.7 | Hip motor torques specified by the controller | 79 |

| | | |
|-----|--|----|
| 5.8 | Plot of data points of the required torque/speed pairs from the knee joint and prospective motor operating ranges to assess feasibility. . | 80 |
|-----|--|----|

ABSTRACT

Legged robotics have proven to be a viable approach to extending human reach to various terrains that are unfit for conventional wheeled locomotion. While advances have been made to further capacity of these robots through a variety of design approaches, there are still difficulties in bridging compromise between energetic efficiency and joint dexterity. Switchable Parallel Actuators (Sw-PEAs) have been proposed and developed in legged robotics to address this trade-off by providing the benefits of both control authority of the joint, and passive compliance, in a manner that is desired by the overall objective of the application.

This thesis begins by building upon the Sw-PEA concept, by first discussing a two-link monopodal robot, SPEAR-II, which is the second design iteration of the robot SPEAR (Switchable Parallel Elastic Actuator Robot). A mathematical model of the monopod is created with a focus on understanding the internal system interactions to use for simulation and controller design. Parameter identification experiments are then conducted to improve the accuracy of the model by estimating previously unknown variables. Using the refined monopod model, a simple controller is tuned and implemented on the robot during hopping experiments. Lastly, a quadruped design is proposed using SPEAR-II as a legged template. A quadruped model is derived to perform analysis on key design parameters. Finally, the thesis concludes with results for the quadruped simulation as a feasibility study for the proposed design using the Sw-PEA.

Chapter 1

INTRODUCTION

1.1 Motivation

Legged robots have the potential to extend our reach to terrains that challenge the traversal capabilities of traditional wheeled platforms [36]. To realize this potential, diverse legged robot designs have been proposed, and a number of these robots achieved impressive indoor[12] and outdoor[37] terrain mobility. However, combining mobility with energy efficiency is a challenging task due to the inherently dissipative nature of legged locomotion[22]. Furthermore, legged robots typically operate in regimes where the natural dynamics of the mechanical system impose strict limitations on the capability of the actuators to regulate its motion [39]. To address these challenges, a series of actuator designs have been introduced, the majority of which combine elastic energy storage elements with motors to generate and sustain locomotion.

In the context of robots powered by electric motors, compliance is commonly implemented to provide desired benefits. One widely adopted approach is the Series Elastic Actuators (SEAs) [35], which introduces compliance in series with the motor. A variety of robots successfully employ this actuator architecture, including bipeds [17, 15] and humanoids [24], as well as quadrupeds [19]. Conversely, another less common actuator configuration is the Parallel Elastic Actuators (PEAs) [49], where a compliant element is placed in parallel with the motor. With this configuration, an attractive feature is that the spring provides most of the torque required at the joint to maintain a desired motion. Additionally, the motor can modify the torque profile as needed to stabilize the system [29]. However, a drawback to introducing springs in parallel with the actuators is that they may limit joint mobility. This is due to the fact that

the spring may interfere with the motor even when it is not needed [13]. This fact possibly explains the scarcity of robots using PEAs. One approach to overcoming this drawback is the idea of inserting a switchable spring in parallel with an actuator has been mentioned in [29]. While a few prototypes that combine parallel elasticity with switching mechanisms have been proposed as standalone actuation units [13, 32, 28, 10], the effectiveness of Switchable Parallel Elastic Actuators (Sw-PEAs) is ideally shown in a legged locomotion setting consisting both monopedal applications [26, 25, 27], and quadrupedal locomotion.

1.2 Literature Review

In the context of electrically actuated systems, one approach to increase energy efficiency is to use regenerative braking to capture some of the energy when the motor is performing negative work [42]. Using this method, the MIT cheetah[43], with its customized high torque density motors, displayed impressive locomotion efficiency [44] and light legs[2]. Through regenerative braking, where electrical energy is recaptured by the specially designed motor driving circuitry, it eventually needs to be converted back to mechanical energy[32]. Due to the large torques involved, and the ensuing losses from Joule heating, energy conversion occurs at a low efficiency for legged robotics applications. This has been shown in [42], where a 24% conversion efficiency is reported with optimally designed motors.

As an attempt to mimic the naturally compliant structures in the legs of animals[1], such as muscle fibers and tendons, mechanical springs have been demonstrated as a way to recycle energy into legged robot designs [47]. Nature is rather successful in recycling energy, as tendon efficiency can reach up to 90% [33]. However, mechanical approximations, such as steel springs, could have an even higher number due to low hysteresis [18, p. 142].

In addition to energy recycling, benefits such as reduction of the peak power and torque requirements of the actuators can be achieved using strategically inserted compliant elements [11]. By reducing the actuator requirements, efficiency further

improves by having the actuators operate in a low torque region, where the efficiency of electromagnetic motors increases as the output torque decreases [14]. The introduction of compliant elements in legged robots have shown success in improving energy efficient by placing the compliant elements in torsos [5, 4], as well as placement in the legs [34].

One approach to introducing compliance within the legged robot’s structure is by placing a spring in series with an actuator, in what is known as the Series Elastic Actuator (SEA) [35, 47, 30]. In the realm of legged systems, one of the earliest implementations of series compliance can be found in Raibert’s robots, where air springs were placed in series with hydraulic actuators [36]. The bipedal robot MABEL realizes spring-mass walking [45] and running [46] through its design using large leaf springs connected in series with the actuators through a transmission system. This ensures that compliance is present in the leg length direction [16, 17]. In recent years, ATRIAS hosts a series-elastic parallelogram mechanism to demonstrate 3D spring-mass hopping and walking motions [15]. The humanoid COMAN [24], follows a different philosophy of this actuation approach, and is powered by intrinsically compliant knee and ankle joints. Additionally, the quadruped StarLETH is constructed using 12 SEAs actuating all of its joints [18]. SEAs, in addition to providing passive mechanical energy storage [16, 17, 15] and torque control capabilities [18, 30], offer a means of protection for the motor and gearbox by filtering out impulsive loads at collisions and impacts, and therefore have some ideal properties for legged locomotion.

However, there is a tradeoff with these benefits as the motors in SEAs must have the capacity to produce torques and forces that are comparable to ones being generated by the springs [3]. For the applications of dynamic legged robots, this translates to the design of robots that require large motors and gear reduction ratios. What is more, SEAs commonly increase the number of degrees of freedom (DOF) of the system, due to the relative displacements between the actuator and end-effectors, and can require special design and control considerations [20, 30]. Mentioned in [40], compliance in series with the actuator may limit the range of behaviors realized by the system. One

approach to actively modify the stiffness of the passive component, has been shown using a variable stiffness actuators (VSA). This design can help mitigate this restriction, however, many current VSA designs tend to increase the complexity of the system. A review of VSAs can be found in [47].

In contrast to SEAs, another approach to introduce compliance, is using Parallel Elastic Actuators (PEA), in which the spring is inserted in parallel with the motor so that the spring and the actuator work in an additive fashion [29]. One example of using a design using PEA is found in [3], where springs not only improve energy efficiency but also increase the safety of known maneuvers in passive-assist devices for active joints. The biped ERNIE illustrates a legged robot application of a PEA by utilizing springs in parallel with its knee actuators to generate walking motions [49]. The additive nature of the spring and actuators, in PEAs, may reduce both power and torque requirements. This is suggested by simulations of bipedal [11, 8], as well as quadrupedal [9] running. Prosthetic applications have shown this effect as well in [48]. As with every compliance-oriented actuator design, there is an inherent tradeoff. By introducing springs in parallel with the actuators, the joint dexterity may be limited since the actuator needs to work against the spring [13]. In recent years, numerical optimization found in [50] has investigated the optimal actuation configurations among different combinations of SEAs and PEAs controlling a two-dimensional hopping model. The findings are that the optimal actuation configuration, based on the metric of positive electrical work, is dependent on velocity.

An increasing number of actuator designs have begun to incorporate discrete coupling elements, such as clutches or brakes, into the SEA concept to address some of the drawbacks previously discussed [31]. These coupling elements can increase the output performance of the actuation unit. For example, in [38], a clutchable SEA is developed, where the clutch is put in parallel with the motor. The spring is allowed to deform, when the clutch engages, by connecting one end of the spring directly to a fixture. This allows the motor to be bypassed, and hence it does not need to produce any torque. Another example is found in [38], a design within an active knee

prosthetic device, where the observed energy consumption is an order of magnitude less than previous results. One downside is that the motor is unable to provide additional energy when the clutch is active. A general purpose SEA found in [23], utilizes discrete coupling elements to achieve multimodal operation for versatile applications. The prototype actuator is suitable for relatively large systems, measuring in at 0.67m long and weighing 4.5kg.

In an analogous approach, discrete coupling elements can also be used to overcome the drawbacks associated with PEAs. The work in [29], which analyzes a planar bipedal walking model, advocates the use of a Switchable Parallel Elastic Actuator (Sw-PEA) using a position-dependent clutch. This function would enable the spring to be engaged where it is most desired, while a leg is in stance, but not during flight. A similar observation in the context of modeling high-speed quadrupedal running is made in [9]. However, it is noted in [9], that generally speaking, commercially available clutches are slow and typically have undesirable size and weight for legged robotics applications. Furthermore, the authors propose a conceptual design for realizing switchable compliance in the context of the MIT Cheetah’s leg design [2].

Outside of simulation studies, only a few hardware prototypes exist that combine PEAs with switches. One such prototype described in [13], uses a clutch to as an effective switching mechanism. An alternative approach proposed in [28], develops a prototype of an actuator which recruits several parallel elastic elements in sequence with mutilated gears, using a single motor. The maximum output torque of the actuator is increased in this arrangement. Furthermore, in a more recent version found in [10], the design allows for stiffness adjustments. However, the complexity of the current prototypes is higher relative to other actuator designs. A bi-directional Sw-PEA prototype is presented in [32], which implements a differential consisting of two locking mechanisms to load and unload the spring in a controlled manner which reduces energy consumption.

Prior to work shown in [26], there are a few results in exoskeleton design, which hosts a mechanical clutch [7] or electrostatic forces [6] to engage and disengage the

parallel spring. Furthermore, the design of a dynamic bipedal robot that employs a Sw-PEA at its knee joint is presented in [21], and offers a preliminary energy analysis. The development of SPEAR, a monopedal robot using a Sw-PEA at the knee joint, has demonstrated effectiveness of the concept in practice as well as the energetic benefits are found in [26, 25]. The observations of the discussed research inspires the future steps of implementing the Sw-PEA in a quadruped application.

1.2.1 Summary of Contributions

The contributions of this thesis can be summarized as an overview below.

- Robot design of an implementation of the Sw-PEA actuator in a new revised design of SPEAR. The new design was developed with the intention of creating a template for a quadrupedal implementation of the Sw-PEA actuator.
- Higher resolution model of the interactions and dynamics of SPEAR-II, and a parameter identification technique to further understand details related to the improved design.
- Model and analysis of a Sw-PEA leg design, and SPEAR-II template, in a quadrupedal design. Fixed points for periodic bounding gaits are found for this model.

1.3 Organization of the Thesis

The thesis is organized into three chapters describing the associated work, and ends with a chapter providing a summary of the findings, as well as a discussion of future work. Chapter 2 familiarizes the reader with the concept of the Sw-PEA, and the robot SPEAR. The chapter then discusses the design of the robot of interest for this work, SPEAR-II, a second iteration of SPEAR. Chapter 3 provides the details to the mathematical model used to describe the system. Chapter 4 builds upon the model of SPEAR-II and describes parameter identification experiments to fine-tune the model. The results are then used to simulate the monopedal robot and design a controller for hopping-in-place. Chapter 5 uses the SPEAR-II model as a legged template for a proposed quadruped robot. The model of the newly conceived quadruped is then simulated using an established bounding gait controller to assess the feasibility of the

SPEAR-II design for the quadruped application. Chapter 6 concludes with a summary of the thesis, and a discussion of potential future work.

Chapter 2

SPEAR-II: SECOND ITERATION OF SPEAR

2.1 Concept of Sw-PEA

In addressing the challenge of possessing both joint mobility and energetic efficiency in legged locomotion, a large effort is devoted to design of the actuator and its hardware realization. Incorporating necessary compliance is a challenging task, when trying to maintain a high degree of control authority in the mechanical system. Desired features of an ideal leg design in the context of mobility and energy-efficiency for legged locomotion would include the ability to store and recycle energy during stance phase and impact, and simple, unimpeded control of joints while in flight phase.

To address this tradeoff, the actuator design of Sw-PEA, Switchable Parallel Elastic Actuator, is proposed. The benefit of this concept is that it engages compliance in parallel with the actuator only when energy storage is needed. When storage of energy is not necessary or desired, the design does not interject compliance and thus allows the motor to control the joint as specified.

2.2 Sw-PEA in a Monopod Setting

As a more concrete illustration of the benefits of the Sw-PEA mechanism, consider a legged robot application of the actuator. For a 2 degree of freedom (DOF) leg (hip and knee joints), the Sw-PEA design would be effective at the knee joint where compliance can store energy during the stance phase where the leg contracts and the knee actuator performs negative work. To better understand the concept behind the mechanism, consider the schematic in Fig. 2.1. The Sw-PEA actuator exists between Link A and Link B. S_1 is a stiff spring, and S_2 is a soft spring with negligible stiffness that is solely used as a return spring for alignment.

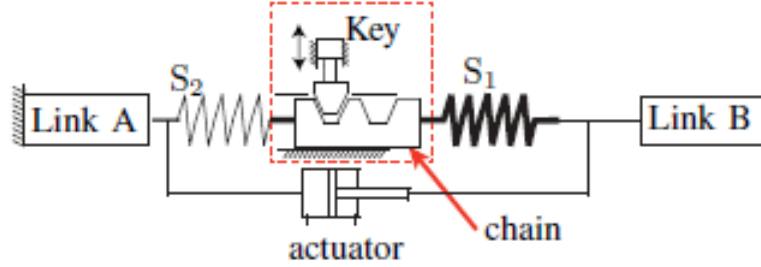


Figure 2.1: Schematic of Sw-PEA mechanism design. Switching the key by engaging/disengaging into the chain, changes the stiffness at the joint from K_1 to K_2 . Shown in [25]

When the mechanical key is engaged, the soft spring, S_2 , is no longer effective and the stiff spring, S_1 , is in parallel with the actuator. The system now behaves as a PEA mechanism, and disturbances to the position of Link B will be resisted by the spring S_1 , requiring little, if any, control effort by the actuator. When the mechanical key is disengaged, the two springs are in series with each other, and both are in parallel with the actuator. With the two springs in series, the effective stiffness is that of the smaller spring, S_2 , which is negligible; Therefore, the actuator can move Link B without having to do work against the stiffer spring S_1 .

Analogously, in a monopodal setting, one implementation of the Sw-PEA is to have the switch (key in Fig. 2.1), located at the foot as a passive mechanical switch. This synchronizes the engage/disengage feature of the key with the natural motion of hopping, without requiring additional actuation to change the stiffness of the parallel elastic actuator (PEA). Shown in Fig. 2.2, the foot of the monopod has a tooth (key) that engages the chain when the ground reaction force is essentially greater than zero (i.e. stance phase, and landing/impact). With the key engaged, the mechanical switch is considered on and spring S_1 , the stiff spring, is acting at the knee joint in parallel with the motor. This allows for storage and utilization of impact energy throughout the stance phase, and thus little to no control effort is required by the knee motor.

In contrast, when the leg takes off from stance phase and is in flight phase, the

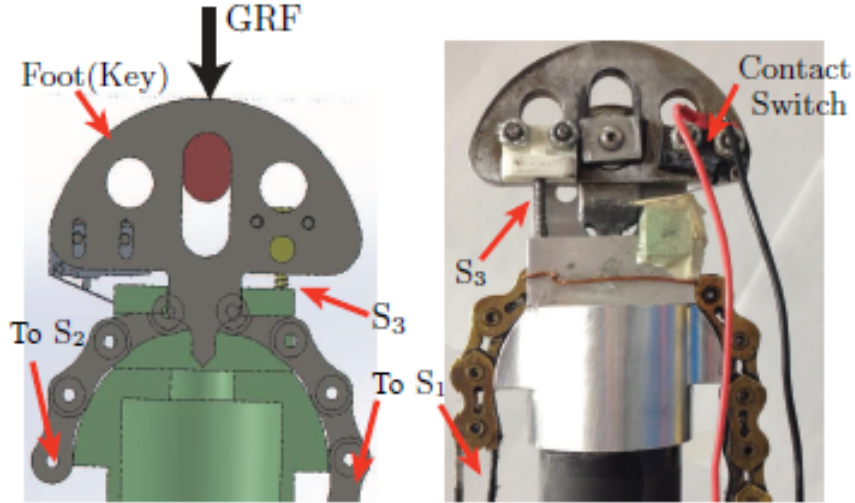


Figure 2.2: Left: CAD model of Sw-PEA mechanism at the monopod foot. Right: Photo of SPEAR foot to implement the Sw-PEA at the knee joint of the robot. Note that the spring S_3 is a small spring with negligible stiffness, and is used to prevent binding with the key and chain. Shown in [26].

foot (key) is released and disengaged by the ground reaction force going to zero (spring S_3 in Fig. 2.2 acts to prevent binding and allow the foot to release). While the switch is off, the stiff spring, S_1 , is not engaged to the knee since it is in series with spring S_2 and $K_2 \ll K_1$. The result is that the knee motor can provide control over the joint without having to work against the stiff spring, S_1 , and only needs to overcome spring S_2 , which has a negligible stiffness.

The resulting benefits of utilizing the Sw-PEA design in a monopod setting, is that the efficiency of legged locomotion can be greatly improved in comparison to other legged robot implementations of PEAs and series elastic actuators (SEAs). The energy is stored during the compression portion of the stance phase, and can be recycled throughout the gait, without requiring a large control effort from the actuators. Additionally, during flight phase, when position control is desired, the passive compliance of the knee joint is removed from the system to allow the actuators to implement position control with effort minimized.

2.3 SPEAR: First Iteration

SPEAR, Switchable Parallel Elastic Actuator Robot, is a legged robot that uses a Sw-PEA at the knee joint. SPEAR (also referred to as SPEAR-I in this thesis) is a planar monopodal robot that is comprised of two links, thigh and shank, and two independent and fully-actuated joints acting as the knee and hip. Fig. 2.3 shows a photograph of SPEAR-I with key components related to the robot and the Sw-PEA shown.

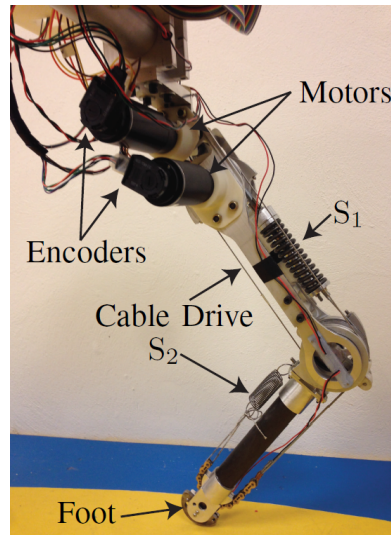


Figure 2.3: Image of SPEAR-I leg depicting the various components of the Sw-PEA mechanism introduced into the leg design; see [26].

The robot uses two servomotors one directly at the hip joint, and the other effectively at the knee joint. The knee motor controls the shank angle through a rigid cable pulley system. The design hosts a passive mechanical switching mechanism that allows for a stiff spring to store energy from compression during stance to be recycled during the push-off phase in preparation for liftoff. While the leg is in flight phase, however, the mechanical switch is effectively unlocked and disengages the spring from the knee joint, allowing the actuator to control the joint position without interference from the stiff spring.

The benefit of utilizing a Sw-PEA in a monopod is demonstrated by the experimental results of SPEAR-I. A common metric to assess energy efficiency in legged systems is the cost of transport (COT), where a lower COT value represents higher efficiency. Fig. 2.4 is a plot comparing the COT of various animals and legged robots. The variety of animals are represented by the circular indicators, whereas the robots are represented by squares on the plot. The red square at the center of the plot represents the values for SPEAR-I. Note that SPEAR-I is located on the green trendline representing running animals, indicating that the Sw-PEA creates locomotion comparable to legged systems in nature.

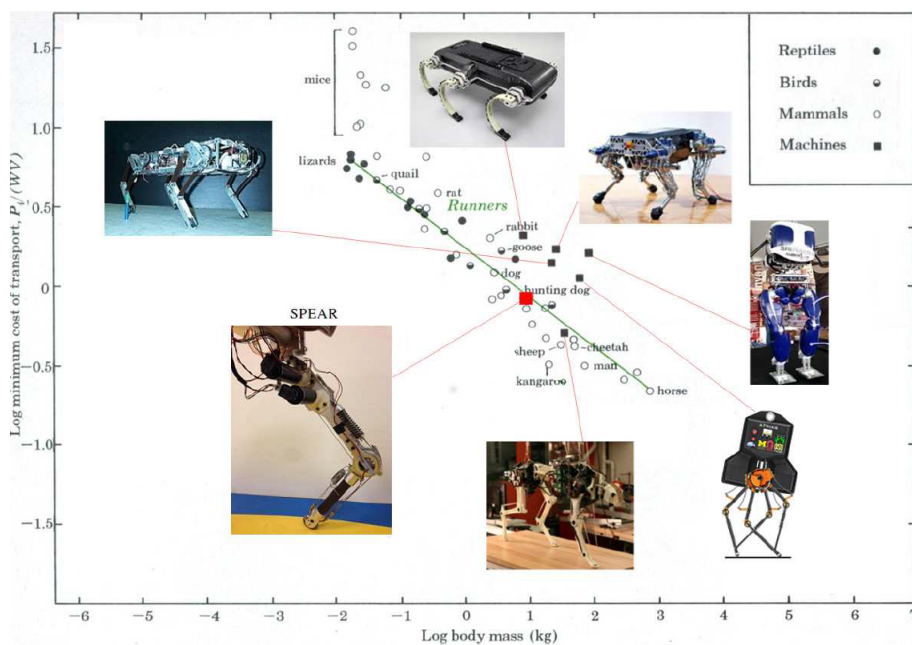


Figure 2.4: Log-Log plot showing the cost of transport (COT) vs body mass of various robots and animals. The values for SPEAR-I are plotted to show comparison with other robots and animals; see [27].

Following the outcomes of the SPEAR-I monopod design, an interest in creating a quadruped using the SPEAR-I as a leg template pursued for the next step. However, in the early stages of this effort, desirable improvements were made evident to successfully implement a Sw-PEA in a quadruped. An example of an improvement is seen in Fig. 2.5. This figure illustrates two CAD renderings of conceptual layouts of

a quadruped design using SPEAR-I as a leg template. One issue that is visible in the figure is the geometry and footprint of the leg. Notice that the knee motor (below the hip motor) will likely cause interference when the angle of the thigh changes, and can potentially collide with another part of the quadruped.

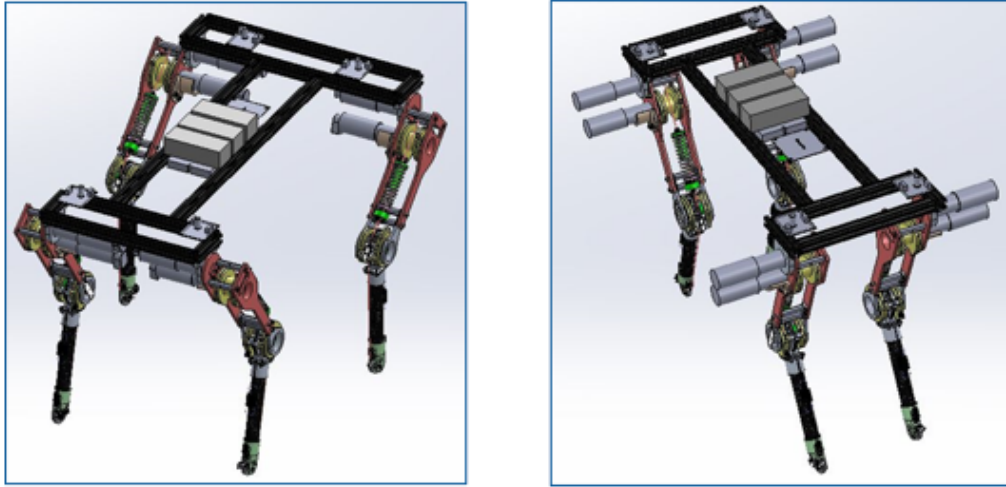


Figure 2.5: 3D CAD renderings of a conceptual quadrupedal robot using the SPEAR-I legs in the design.

Through the early assessment of planning a quadrupedal SPEAR-I robot, the initiative to improve the design was prompted. The redesign effort resulted in a new version of SPEAR, called SPEAR-II.

2.4 SPEAR-II: Second Iteration

The second iteration of SPEAR, or SPEAR-II, was designed with the intention of creating a monopedal platform which can be used as a legged platform to create a quadruped. Overall, the following design objectives are required:

| Improves Dynamics | Improves Functionality |
|---------------------------------------|---|
| <i>Weight Reduction</i> | <i>Packaging of components</i> |
| <i>Inertia Reduction</i> | <i>Foot (Sw-PEA Switch) Reliability</i> |
| <i>Dynamic Balancing at Hip Joint</i> | <i>Geometry and Footprint</i> |

Table 2.1: Overview of the design improvement goals for SPEAR-II.

Fig. 2.6 shows the 3D CAD model of SPEAR-II (on the left), with a photograph of the hardware realization of the design. The image of the model rendering highlights the slider design on the boom of the robot. The leg is free to move in the up and down direction for hopping, with the steel shafts guiding the ball bearings throughout the motion.



Figure 2.6: Left: 3D CAD Model Rendering of the SPEAR-II design with slider boom. Right: Photo of SPEAR-II robot in stance phase.

A side-by-side comparison of the two leg designs are illustrated in Fig. 2.7. Notice an example of the change in overall material selection where the aluminum plates used in SPEAR-I are replaced with carbon fiber tubes as much as possible.

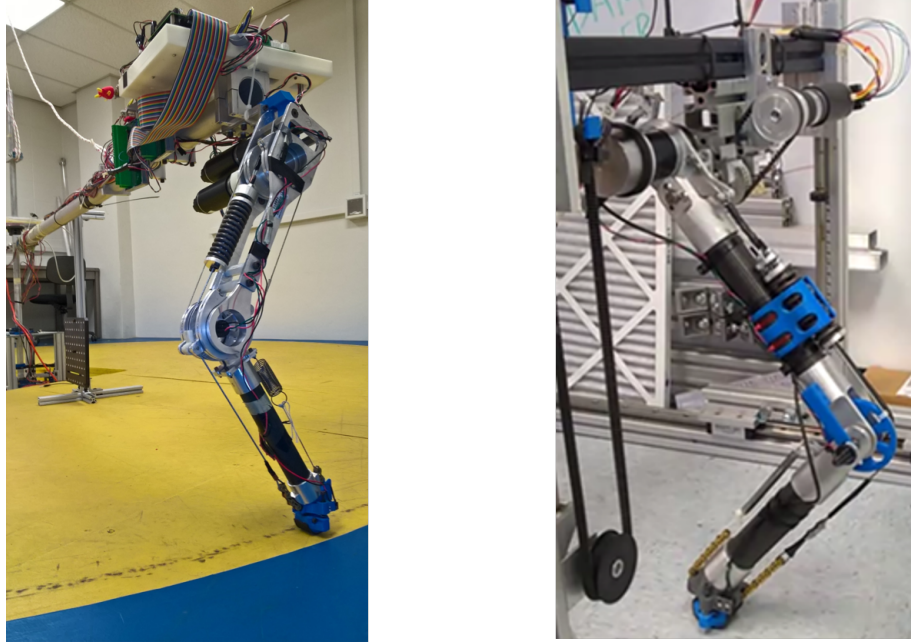


Figure 2.7: Left: Photo of the first iteration of SPEAR; see [27]. Right: Photo of the second iteration of SPEAR (SPEAR-II)

To address the desired improvements in list shown in the previous section, a set of relevant design metrics are identified to quantify the improvements in the SPEAR-II design. These parameters set forth are specific to the improvements and are assessed relative to the SPEAR-I design parameters. Below in Table 2.2, these parameters are tabulated along with the corresponding values for SPEAR-I. Notice that most are centered around the mass and inertia of the links. Additionally, form factor and footprint of the leg are capture by the metric of thigh width, and the dynamic balancing feature is measured by the location of the center of mass of each link relative to the corresponding joint.

| Parameter | SPEAR | |
|----------------------------|-------|------------------------|
| | Value | Units |
| Leg Mass | 4.55 | <i>kg</i> |
| Thigh Mass | 3.6 | <i>kg</i> |
| Shank Mass | 0.95 | <i>kg</i> |
| Thigh Link Inertia | 0.039 | <i>kgm²</i> |
| Shank Link Inertia | 0.02 | <i>kgm²</i> |
| Hip Motor Inertia | 0.047 | <i>kgm²</i> |
| Knee Motor Inertia | 0.008 | <i>kgm²</i> |
| Thigh COM distance to Hip | 0.092 | <i>m</i> |
| Shank COM distance to Knee | 0.097 | <i>m</i> |
| Hip Gear Ratio | 60:1 | unitless |
| Knee Gear Ratio | 25:1 | unitless |
| Thigh Width | 0.081 | <i>m</i> |

Table 2.2: Table showing the relevant design parameters and values for SPEAR-I. These parameters are used for assessment of the redesign effort in creating SPEAR-II.

2.4.1 Knee Motor Change

A major design decision for the second iteration was to move the location of the knee motor, as well as change the selection of motor type and gear ratio. In SPEAR-I, the cylindrical-shaped Faulhaber motor that drove knee joint was placed below the hip joint, and was on the medial side of the leg (if it were considered to be a quadruped). This design decision had repercussions with regards to the location of the center of mass of the thigh, as well as range of motion of the leg.

The differences in motor sizes can be seen in Fig. 2.8. The figure shows a 3D CAD model of SPEAR-II, with a focus on the motors on the robot. On the left side of the image, the compact pancake motor for the knee joint mounted on the thigh. On the right, the long cylindrical motor used at the hip joint is shown mounted to the boom. The hip motor for SPEAR-II has the same motor dimensions of the knee motor in SPEAR-I. Fig. 2.8 highlights that the length of the knee motor is nearly half of that of the hip motor. This design selection was deliberately made to reduce the overall footprint of the leg design.

The longer, cylindrical Faulhaber[®] motor had better rotor inertia properties

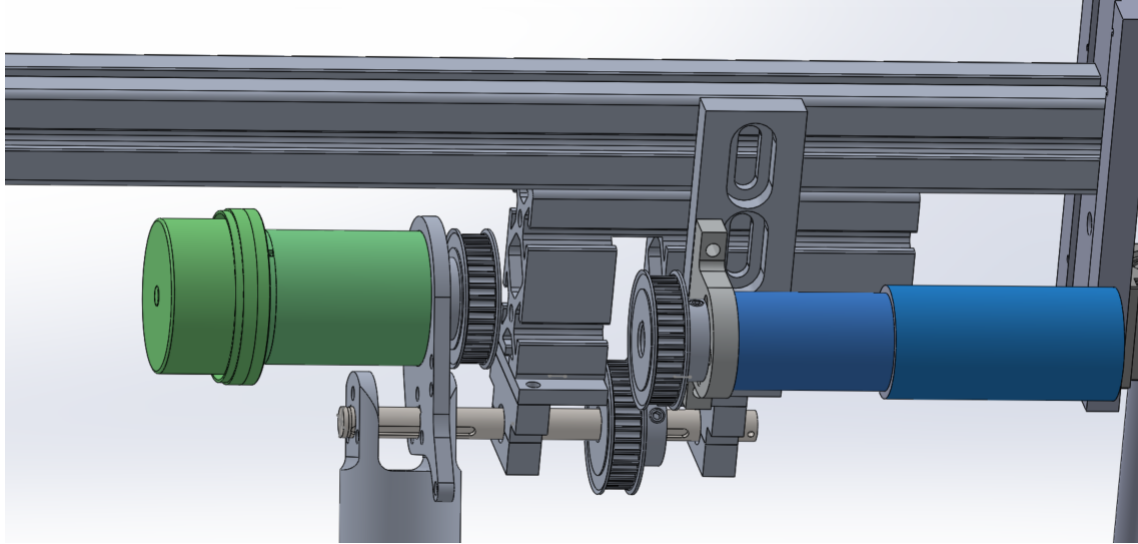


Figure 2.8: The figure is a screenshot of the 3D CAD model of SPEAR-II to illustrate the geometric differences of the newly implemented Maxon[®] motor (green coloring), and the previously used Faulhaber motor (blue coloring).

due to its design with the coils being more spaced out and less densely placed, and the mass distribution of the rotor being closer to the axis of rotation (cylinder shape). While this is beneficial from a dynamics and efficiency perspective, the geometry of the motor and gearbox causes limitations in range of motion in a quadrupedal application. To address this drawback, a new motor was selected to drive the knee joint, and thus the position of the shank. A Maxon[®] EC-60 Flat 100W Brushless DC Motor with a Maxon[®] Planetary Gear Head using a 15:1 speed reduction ratio.

Relocating the placement of the newly selected motor in SPEAR-II also addresses the design improvement objective of dynamic balancing of the hip joint. Shown in Fig. 2.9, the placement of the Maxon[®] motor on the opposite side of the hip axis to the thighs inherent COM moves the overall upper leg COM closer to the hip axis. In the figure, the diagram on the left is representative of the thigh COM on the SPEAR-I leg, which is located approximately 9.2cm from the hip axis along the thigh direction. The improved design layout and selection of the knee motor moves the upper leg COM to approximately 8mm from the hip axis in SPEAR-II.

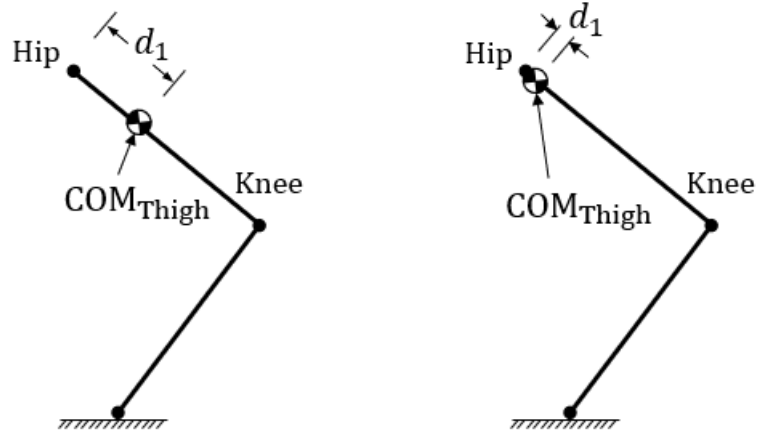


Figure 2.9: Diagrams of the locations of the thigh COM both SPEAR-I (left), and SPEAR-II (right). Notice the effect of improved dynamic balancing by relocating the knee motor to be above the hip axis.

2.4.2 Mass and Inertia Reduction

Reducing the weight of the materials used in the leg helps to reduce the mass moment of inertia at each of the joints. Through careful design and consideration regarding material selection, manufacturing, and geometry, the mass properties were significantly reduced in the second iteration of SPEAR. Additionally, with the placement of knee motor on the opposite side of the thigh's natural center of mass (COM), the new COM of the thigh for SPEAR-II is closer to the hip joint axis, thus reducing the mass moment of inertia about the hip.

With the goal of designing parts which will greatly reduce the mass and moment of inertia of the legs, the design phase was initiated by looking at aspects to improve upon in the original design of SPEAR-I. Components that added mass and complexity, such as the knee pulley mechanism, were re-designed to reduce the mass properties of the leg while also maintaining the required strength to withstand the dynamic loads from impact during landing, as well as applied torques during the stance phase. With SPEAR-I, the knee torque is transmitted through a cable-driven pulley mechanism

which was designed and custom-built for the bi-directional application, and with high-strength stainless steel cables.

The updated transmission mechanism, on SPEAR-II, is shown in Fig. 2.10. This figure displays a close-up photograph that is focused on the two timing belt transmission systems, for the knee and hip joints. On the left side of the figure, the newly selected Maxon[®] motor drives the shank, and correspondingly the knee joint angle, through the attached timing pulley and belt system. This is identified in the figure by the yellow textbox and arrows. On the right, is the Faulhaber hip motor with the corresponding belt transmission, highlighted by the green textbox and arrows.

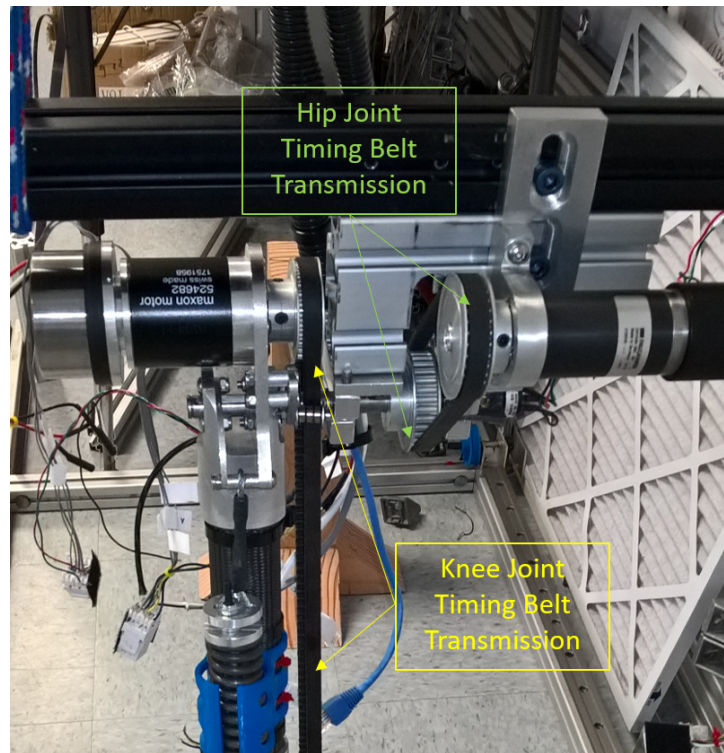


Figure 2.10: Photo focused on the timing pulley torque transmission mechanisms for SPEAR-II.

The tension that is applied to the knee's timing belt is done so by using a roller bearing mechanism (seen near the hip shaft on the belt), which is pressed down onto the belt by a mechanical lever which is fastened in place using two steel bolts. The

tension on the hip belt is created by sliding the plate which mounts the motor in the upward direction, and then fastening the large blue bolts on the boom (shown on the right side of the figure, above the motor). Note that Fig. 2.10 is the hardware realization of the 3D rendering shown in Fig. 2.8.

In SPEAR-II, the knee torque is transmitted through a more standard timing belt pulley mechanism. The belt is a GT-2 tooth profile, 9mm wide, neoprene timing belt reinforced with glass fibers, capable of handling loads much greater than the applied torques and impulses. With the standard, off-the-shelf, timing belts and pulleys available, the design is not only effective in reducing weight but also is a lower cost alternative to the custom-made cable-drive pulley system. However, the improvements also come with a tradeoff in that a tensioner mechanism is required for a timing belt transmission. The added requirement of tension not only comes with some additional design complexity (to make the tensioner compact and effective), but increases damping through friction from the added force from the tensioner. An additional benefit of the timing pulley design is the reduced design complexity of the overall thigh. With SPEAR-II, the thigh structure is simplified further by using an off-the-shelf, thin-wall, woven carbon-fiber tube with aluminum caps bonded to it. This reduces weight and rotational inertia in comparison to the previous design using parallel aluminum plates, with the cable-pulley transmission mechanism in between.

2.4.3 Toe and Foot Redesign

By far, the most challenging component to design on SPEAR-II (and SPEAR) is the toe and foot assembly. In the Sw-PEA mechanism, the toe acts as the mechanical switch which changes the stiffness of spring S_1 to S_2 . The design challenge consists of creating parts that can withstand the relatively large loads and impulses by both the spring in the Sw-PEA as well as the impulsive interactions with the ground and reaction forces. Additionally, since the toe and foot assembly is the farthest part of the leg from the hip axis, the components need to be relatively light-weight to reduce the inertia of the leg.

In the first iteration of the robot, the toe had a complex geometry and was made out of steel. Furthermore, the chain was made using off-the-shelf bicycle chain which is also steel (see Fig. 2.2). While the design could substantially withstand the impact forces and impulses from hopping, there were areas in which the design could be improved. As with the rest of the robot design, reducing weight helps create more efficient motion. Also, issues with binding and stiction due too the asymmetric implementation of the release springs, essentially the two springs S_3 in 2.2, were addressed in the subsequent design.

Fig. 2.11 shows the 3D CAD model of the updated foot assembly implemented on SPEAR-II. The design features numerous modifications that help reduce the overall mass of the assembly, and improves the reliability of engaging and disengaging as a switch.

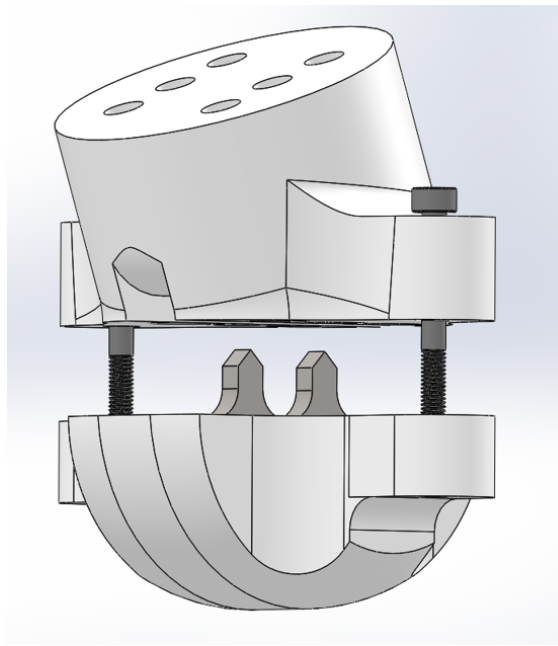


Figure 2.11: 3D CAD Model Rendering of the Foot Assembly on SPEAR-II.

The material selection plays a large role in the improvement of reducing the mass of the assembly. By using primarily PLA plastic (shown as white parts) in the

design, in comparison to the aluminum and steel used in the SPEAR-I foot, the mass is reduced significantly. Due to the high strength requirements of the foot to withstand the spring force of the leg, some parts are still designed using steel. Shown in the figure, the dark grey parts such as the tooth on the foot, and the bolts connecting the upper and lower components are made of steel, but are kept to a minimum. The overall tooth profile and design is conceptually similar to its predecessor (Fig. 2.2), but is improved with reduced weight and better ejection abilities. With the previous foot on SPEAR-I, shown in Fig. 2.2, there were commonly seen issues with the toe not ejecting during flight due to binding, friction, and the asymmetric spring S_3 . In fact, due to the large improvement in reliability, the foot on SPEAR-I was later removed and replaced with a new assembly based on the new design shown in Fig. 2.11.

The design methodology around the new foot concept involved a heavy reliance on Finite Element Analysis (FEA) packages, and trial and error with simulation of the loading of the key components. Since the foot assembly in SPEAR-II is primarily made from PLA plastic using a 3D printer, experimentation with the manufacturing method allowed for a rapid prototype approach to tweaking parameters such as infill percentage, direction of the filament, and adhesive and bonding methods. Eventually the material and manufacturing method was selected to both handle the loading from impact and spring S_1 , while also minimizing weight by reducing the amount of material used. High stress areas such as the shaft inserts and teeth inserts, were designed using steel but consist of very little amount of material. These steel components were fastened to the plastic components using bolts and adhesives. The toe assembly connects to the overall foot assembly through two equidistant bolts which thread into the toe assembly. The symmetry of the two bolts and equal S_3 springs, shown in Fig. 2.11, create a reliable release mechanism to eject the toe from the chain (while in locking position) and ensures that the toe is never stuck in the chain after take-off. A coating of bike chain lubricant is applied to further prevent problems of stiction.

Prior to the final design selection of the foot and toe assembly, multiple variations of the design concept were experimented with trial and error. These concepts

ranged from utilizing a timing belt as the chain component, to implementing a hydraulic braking system as a locking mechanism. The difficulty with implementing many of these designs is the practicality of keeping the design compact and lightweight, while also successfully and reliably operating during hopping motions. Complicated locking mechanisms were many times too bulky to work in an efficient legged robot application. Conversely, light-weight, fully plastic designs would fail under the dynamic loading of impacts and spring forces. Ultimately, the final design reflects a successful trade-off between reliability and functionality, with minimized weight and complexity.

2.4.4 Redesigned Boom

The boom is a critical part of a monopedal robot testing platform. The design of the boom can enable various types of experiments and measurements, and there can be unintended consequences such as added weight, and added friction. An important feature for a boom design is modularity to have the ability to interchange robots. In SPEAR-I much of the boom design was not modular, and involved somewhat permanent attachments of mechanical mounting as well as the wiring of signal cables directly to the robot. This setback resulted in the design of a separate boom for SPEAR-II, and provided the insight of creating interchangeability in the new concept. With the new boom, signal and power wires connecting the robot are achieved through standardized connections, and the attachment mount for the robot itself is connected through simple bolts. This enables the use of the boom for various robot designs in the future by simply disconnecting SPEAR-II, and reconnecting a new robot.

In the first iteration of SPEAR, the boom was designed to rotate in a manner similar to spherical coordinates with a fixed radius. While there is the benefit of relatively low friction at the two revolute joints, the tradeoff is the difficulty in measurement of position and velocity of the hip joint. This is a consequence of the design due to the arc length equation to calculate the position. Essentially, the arm of the boom is a fixed radius of approximately 2 meters in length, and a small error in angular measurement can result in a relatively large error in measurement in the x or y position

of the hip axis. Furthermore, this error can cause additional measurement issues when calculating velocity.

In the second iteration of the monopod, the boom and the attachment of the leg to it was carefully designed to ensure that the ground reaction force would be directly underneath the y -axis slider. In an earlier implementation, the leg was attached to the boom in a way that caused a moment about the vertical sliding mechanism (in the hip axis direction) due to the hip shaft being offset from the sliding access. Through careful analysis of this problem, by reviewing early experiments, the leg attachment component was revisited and redesigned to be more compact, lighter, and with a reduced residual moment.

Various unforeseen complications with the new boom design prompted tweaks to the final design. An example of this is shown in Fig. 2.12, where a previous mounting design concept that was constructed had caused restriction in motion. The figure is a photograph of the SPEAR-II leg mounted to the boom via a long aluminum plate with a tensioner system (the orange plastic assembly with metal ball bearings). While it was less complex in its design, the approach was approximately 30% heavier and caused complications during experiments due to the offset of the hip shaft axis. Notice that the hip shaft is located forward in the x -direction by a distance, d , shown in white on the drawing. This distance was approximately 10cm, and created a moment about the hip axis direction when the leg would interact with the ground. The improved design shown in Fig. 2.10 resolved these issues. The final mount design (shown in Fig. 2.10) for attaching the leg to the boom ensures that the axis of the hip shaft is directly beneath y -direction (linear up/down direction) of the boom. This helps reduce any reaction force moments during hopping, and is discussed more in Section 2.4.4

While the current boom was designed primarily for hopping-in-place experiments, the test bed was designed to enable potential forward motion through an additional horizontal sliding mechanism. An alternative way to use this testbed for running forward hopping experiments could be to strategically install a treadmill underneath the leg, for which there is ample space.

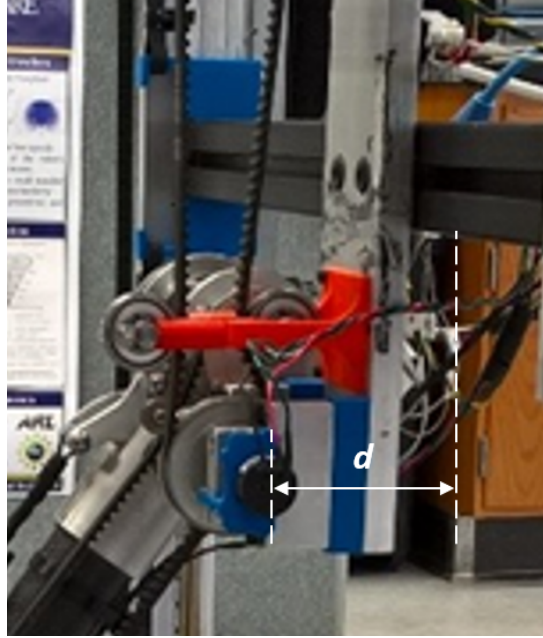


Figure 2.12: Photo of a previous method of mounting the leg to the boom, illustrating the issue of a reaction moment due to the distance offset, d .

2.4.5 Electronics Configuration Details

SPEAR-II has a similar electronic setup to its predecessor. The monopod testbed has the ability to be fully un-tethered and can operate on simply two 24V LiPo (Lithium Polymer) batteries alone. To simplify the implementation of a controller, the electronic hardware selected was chosen for its compatibility with MATLAB[®] Simulink-Realtime[™]. This decision enables rapid prototyping of controller design for experiments in a way that greatly reduces the complications that commonly occur from software and infrastructure bugs.

A diagram showing the electronics used on the robot is shown in Fig. 2.4.5. The system is powered by two 24V batteries. One battery is a power supply to the motors, and the other supplies power to PC-104 CPU stack, peripheral sensors, and motor driver boards. The figure highlights how data is transmitted from the Host PC through the wireless router, and PC-104 stack, using the black lines. The red lines show the electrical flow through the batteries, and the multiple other line colors represent

experiments. Additionally, data from the experiments are stored on the computers hard drive and can be remotely transferred to the host PC to quickly store and review results.

The motor driver takes in reference current as a digital signal and outputs exact current to the motors through its PWM (pulse width modulation) amplifiers. The motor drivers also provide measurement of the current delivered to each motor to be stored as data from the experiments. The motors have 3 phases of power delivered to them, and feeds Hall sensor information back to the motor drivers. Additionally, the motors have encoders that connect with the communications board to provide angular measurement of the motor shaft. Since the encoders are incremental, potentiometers are installed at both the hip and the knee joint shafts to provide absolute measurement of the joint angles. In application, the initial angle of each joint is recorded from the potentiometer measurement and after it is initialized, the angle is measured by adding the incremental encoder output.

2.5 Summary of SPEAR-II Design

Overall, the design effort for SPEAR-II was successful in achieving the goals discussed in Table 2.1. Below, Table 2.3 summarizes the desired improvements and connects them with the design modifications that resolved them. Additionally, it is important to note, and be aware of, the drawbacks associated with these design changes. While they are minor in comparison to the value of the improvements, they can still have an effect on the dynamics of the robot. These design consequences are the larger rotor inertia from the new knee motor, and the added friction due to the timing belt tensioners and increased contact surface area of the boom.

Table 2.3: Table highlighting the desired design specifications, SPEAR-II improvements, and tradeoffs (drawbacks) due to design decisions that were made.

| Design Objectives | Design Improvements | Design Tradeoffs |
|-------------------------|----------------------|--------------------|
| Weight Reduction | Material Selection | Added Friction |
| Inertia Reduction | Transmission | Knee Rotor Inertia |
| Dynamic Balancing | Knee Motor Location | |
| Packaging | Knee Motor Selection | |
| Foot/switch Reliability | Foot Redesign | |
| Geometry/Footprint | Compacted Design | |

Table 2.4 quantifies the design metrics of the desired improvements and compares them with the values of SPEAR-I which were previously shown in Table 2.2. The mass of the leg in SPEAR-II is less than half of the design’s predecessor, as well as the thigh link’s mass moment of inertia. The distance from the hip axis to the thigh link’s COM is reduced from $9.2cm$ in SPEAR-I, to $8mm$ in SPEAR-II, which is largely due to the placement of the knee motor to be opposite of the material COM

(dynamic balancing). The mass moment of inertia for the shank is a slight improvement in the new design, however, this is largely due to the shank in SPEAR-I being constructed primarily with a carbon fiber tube. A form factor metric, the thigh width, illustrates the improvement of the overall reduction of the leg footprint and geometry. This improvement was largely due to the design change of the knee transmission from the bulky cable-driven system to the compact timing belt approach. Some of the design drawbacks are highlighted by the knee motor inertia, where the new flat Maxon[®] motor has a larger rotor inertia than the previously used long cylindrical Faulhaber motor.

Table 2.4: Tabulation of significant parameters for the SPEAR-II leg.

| Parameter | SPEAR | | SPEAR-II | |
|----------------------------|--------------|------------------------|-----------------|------------------------|
| | Value | Units | Value | Units |
| Leg Mass | 4.55 | <i>kg</i> | 2.2 | <i>kg</i> |
| Thigh Mass | 3.6 | <i>kg</i> | 1.72 | <i>kg</i> |
| Shank Mass | 0.95 | <i>kg</i> | 0.48 | <i>kg</i> |
| Thigh Link Inertia | 0.039 | <i>kgm²</i> | 0.014 | <i>kgm²</i> |
| Shank Link Inertia | 0.02 | <i>kgm²</i> | 0.014 | <i>kgm²</i> |
| Hip Motor Inertia | 0.047 | <i>kgm²</i> | 0.047 | <i>kgm²</i> |
| Knee Motor Inertia | 0.008 | <i>kgm²</i> | 0.027 | <i>kgm²</i> |
| Thigh COM distance to Hip | 0.092 | <i>m</i> | 0.008 | <i>m</i> |
| Shank COM distance to Knee | 0.097 | <i>m</i> | 0.14 | <i>m</i> |
| Hip Gear Ratio | 60:1 | <i>n/a</i> | 60:1 | <i>n/a</i> |
| Knee Gear Ratio | 25:1 | <i>n/a</i> | 15:1 | <i>n/a</i> |
| Thigh Width | 0.081 | <i>m</i> | 0.057 | <i>m</i> |

Chapter 3

MODEL OF SPEAR-II

With previous understanding of the basic mechanics and interactions of the Sw-PEA in SPEAR, a similar modeling framework can be derived. In the first iteration of SPEAR, a simpler approach was undertaken in the first iteration of SPEAR due to the initial focus being on proving the concept of an Sw-PEA in a legged robotics. In order to gain a deeper perspective into the internal system interactions, a model with higher granularity is needed. In this section the modeling framework for SPEAR-II is described, while in Chapter 3 the parameters in the model are estimated and used for analysis and experiments.

3.1 Mechanical Model of System

From experience with the first iteration of SPEAR, it is well understood that the knee joint is the primary focus of the design. This is due to both the Sw-PEA actuator being implemented at the knee joint, as well as the environmental interactions being directly felt by that joint. With this understanding in mind, it is important to consider higher-resolution details of the mechanical interactions at the knee joint.

Consider the abstraction of SPEAR-II shown in Fig. 3.1. The image on the left is a photograph of the robot, and the schematic on the right is a model of the important physical interactions of SPEAR-II. Each joint has a torque provided by the motor for control, and a passive spring S_1 which is the compliant element of the Sw-PEA; represented by the spring in the thick green line. The stiffness of the belt is label k_{S_1} in the schematic. The Knee Spacer creates a radius about the knee joint which translates the linear spring into an effective torque which rotates the knee joint. Due to the modification of the torque transmission mechanism in SPEAR-II, changing

from cable-driven to timing-belt, there is an assumed elasticity effect in the belt due to the neoprene material. This is captured by the model from the two small springs shown on the thin green belt, and is labeled k_{belt} in the schematic. An assumption of Coulomb friction from the physical interactions of the timing belt system and the motor assembly is made to account for the energy losses during motion. These friction forces are modeled as damping forces, and the damping coefficients are shown in Fig. 3.1 by b_{belt} and b_{gear} .

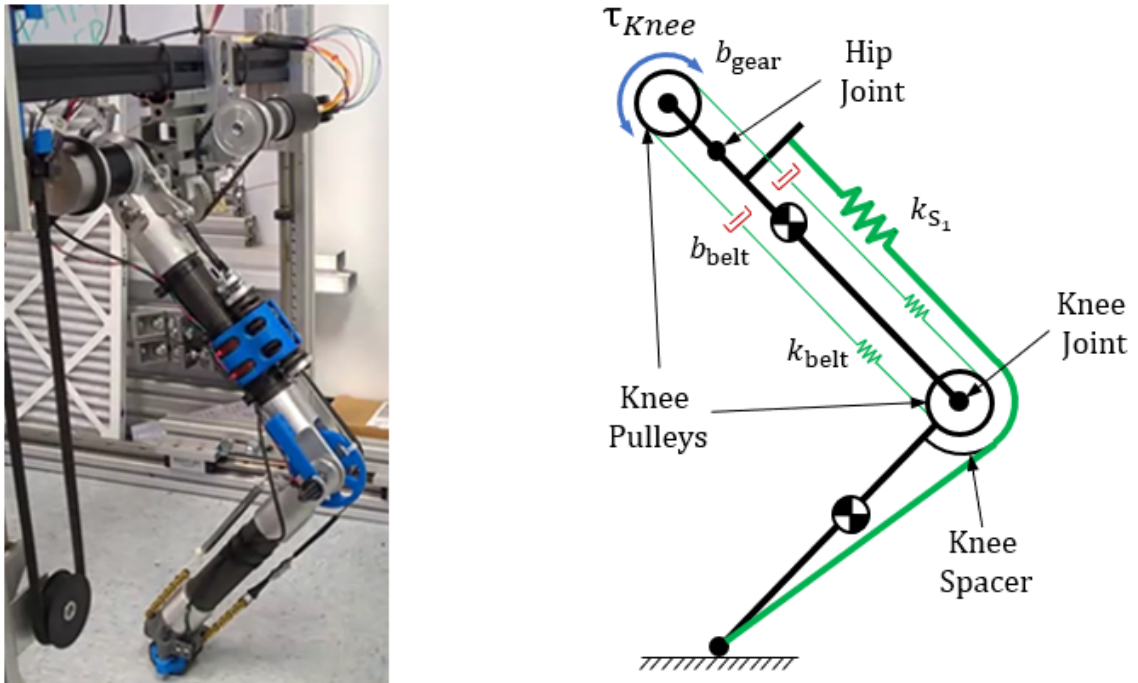


Figure 3.1: Side by side comparison of SPEAR-II with an abstracted model of the important forces at play during the stance phase.

The model is further simplified to consolidate the key interactions into a useful framework that can be used to simulate and design controllers. Since the multiple spring forces acting at the knee joint are in parallel with each other, a single torsional spring stiffness, k_{Rot} , is modeled at the knee joint directly. This can be calculated from taking a summation of the moments about the knee joint. Consider a sum of the

moments from the spring-related forces about the knee joint.

$$\Sigma M_{\text{Knee}} = 2F_{\text{belt}}r_{\text{Pulley}} + F_{S_1}r_{\text{Spacer}} \quad (3.1)$$

where r_{Pulley} is the radius of the timing belt pulleys, and r_{Spacer} is the radius of the Knee Spacer. F_{S_1} and F_{belt} are the linear spring forces from deformation of the timing belt and spring force, of spring S_1 . Following Hooke's law,

$$F_{\text{belt}} = k_{\text{belt}}r_{\text{Pulley}}(\Delta\theta_2) \quad (3.2)$$

and

$$F_{S_1} = k_{S_1}r_{\text{Spacer}}(\Delta\theta_2) \quad (3.3)$$

By substituting, (3.2) and (3.3) into (3.1), we see that

$$\Sigma M_{\text{Knee}} = 2(k_{\text{belt}}r_{\text{Pulley}}(\Delta\theta_2))r_{\text{Pulley}} + (k_{S_1}r_{\text{Spacer}}(\Delta\theta_2))r_{\text{Spacer}} \quad (3.4)$$

$$= (2k_{\text{belt}}r_{\text{Pulley}}^2 + k_{S_1}r_{\text{Spacer}}^2)\Delta\theta_2 \quad (3.5)$$

$$= k_{\text{Rot}}(\Delta\theta_2) \quad (3.6)$$

$$= k_{\text{Rot}}(\theta_2 - \theta_2^{\text{td}}) \quad (3.7)$$

where $\Delta\theta_2$ is the change in knee angle from the equilibrium, this is equivalent to $\theta_2 - \theta_2^{\text{td}}$ which is the difference between the continuous-time knee angle, and the initial knee angle value when the leg first comes into contact with the ground (where the Sw-PEA switch is on and engages the spring). Since belt stiffness effect is relatively small compared to the spring S_1 , it is only significant in the stance phase. The springy effects of the timing belt are negligible in flight phase. Additionally, the damping forces are negligible during flight as well. Lastly, the knee motor assembly and transmission system can be replaced with a torque directly at the knee joint, as well as a corresponding friction force, at the knee joint.

The model of SPEAR-II is shown in Fig. 3.2 and represents the consolidation of the interactions into a lumped spring force, and lumped friction force. The torques from the motors at the hip and knee joint are represented by the blue arrows showing τ_{Hip} and τ_{Knee} , respectively. The lumped rotational spring force is shown by the thick green line labeled k_{Rot} , to represent the rotational stiffness. Lastly, the frictional forces are lumped and modeled as a damping force represented by the red damper diagram, labeled b for the lumped damping coefficient. Note that in flight, the model only considers the motor torques as external inputs to the system.

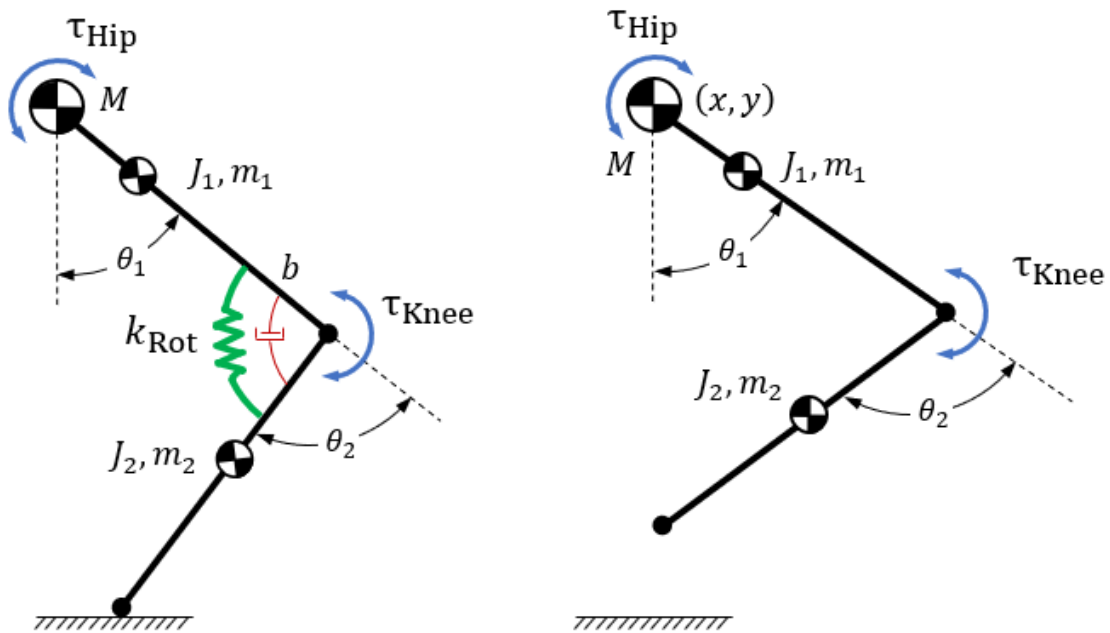


Figure 3.2: Model of SPEAR-II in both stance and flight phase.

3.2 Derivation of Dynamics

Using the model shown in Fig. 3.2, the dynamics are derived using the method of Lagrange by consider the total kinetic energy and potential energy of the system. As an overview of the components of the dynamics equations, a table is provided with relevant parameters for the derivation.

Table 3.1: Tabulation of Dynamics Parameters

| Parameter | Units | Description |
|------------------|-------------------|---------------------------------------|
| M | kg | Mass of the Boom |
| m_1 | kg | Mass of the Thigh |
| m_2 | kg | Mass of the Shank |
| J_1 | kgm^2 | Rotational inertia of Thigh at COM |
| J_2 | kgm^2 | Rotational of inertia of Shank at COM |
| J_{mH} | kgm^2 | Rotational Inertia of Hip Rotor |
| J_{mK} | kgm^2 | Rotational Inertia of Knee Rotor |
| N_{Knee} | n/a | Gearbox Ratio of Hip Motor |
| N_{Hip} | n/a | Gearbox Ratio of Knee Motor |
| d_1 | m | Distance from Hip to Thigh COM |
| d_2 | m | Distance from Knee to Shank COM |
| l_1 | m | Length of the Thigh |
| l_2 | m | Length of the Shank |
| x | m | Horizontal position of Boom COM |
| y | m | Vertical position of Boom COM |
| θ_{mHip} | $\frac{rad}{s^2}$ | Angular position of Hip Rotor |
| θ_{mKnee} | $\frac{rad}{s^2}$ | Angular position of Knee Rotor |

The derivation begins by computing the total kinetic energy of the system. This accounts for both links of the leg, the boom, and the motors (to account for backdrivability effects and reflected inertia).

$$T_{Total} = T_{MotorHip} + T_{MotorKnee} + T_{Thigh} + T_{Shank} + T_{Boom} \quad (3.8)$$

and the potential energy of the system

$$V_{Total} = V_{Boom} + V_{Thigh} + V_{Shank} \quad (3.9)$$

For the Kinetic Energy we see that

$$T_{MotorHip} = \frac{1}{2} J_{mh} \dot{\theta}_{mhip}^2 \quad (3.10)$$

$$T_{MotorKnee} = \frac{1}{2} J_{mk} \dot{\theta}_{mKnee}^2 \quad (3.11)$$

where J_{m_h} and J_{m_k} are the mass moment of inertias of the hip and knee motors' rotor, respectively, and $\dot{\theta}_{m_{\text{Hip}}}$ and $\dot{\theta}_{m_{\text{Knee}}}$ are the angular velocities of the rotors. The relation between the motors' and the joint shafts are related through the gear box ratio by $\theta_{motor} = N_{\text{gear}}\theta_{\text{joint}}$. When substituted into (3.10) and (3.11), we see that:

$$T_{\text{MotorHip}} = \frac{1}{2} J_{m_h} N_{\text{Hip}}^2 \dot{\theta}_1^2 \quad (3.12)$$

$$T_{\text{MotorKnee}} = \frac{1}{2} J_{m_k} N_{\text{Knee}}^2 \dot{\theta}_2^2 \quad (3.13)$$

then, the total kinetic energy is:

$$\begin{aligned} T_{total} = & \frac{1}{2} J_{m_h} N_{\text{Hip}}^2 \dot{\theta}_1^2 + \frac{1}{2} J_{m_k} N_{\text{Knee}}^2 \dot{\theta}_2^2 + \\ & + \frac{1}{2} (J_1 + m_1 d_1^2) \dot{\theta}_1^2 + \frac{1}{2} (J_2 + m_2 d_2^2) \dot{\theta}_2^2 + \\ & + \frac{1}{2} M (\dot{x}^2 + \dot{y}^2) \end{aligned} \quad (3.14)$$

where subscript 1 denotes mass and geometries related to the thigh, and subscript 2 denotes properties related to the shank. J denotes the mass moment of inertias, m denotes masses of each link, M represents the mass of the boom, x and y are the locations of the COM of the boom. The d terms are the distances from the joint axes to the center of mass for each link.

The total potential energy is:

$$\begin{aligned} V_{\text{Total}} = & Mgy + m_1 g(l_1 - d_1) \cos(\theta_1) + \\ & + m_1 g(l_2 \cos(\theta_1 + \theta_2)) + \\ & + m_2 g(l_2 \cos(\theta_1 + \theta_2)) \end{aligned} \quad (3.15)$$

3.3 Dynamics in Floating-base Form

Using the model shown in Fig. 3.2, a convenient choice of generalized coordinates describing the model's configuration is $q := (x, y, \theta_1, \theta_2)'$. Applying the method of Lagrange yields the resulting dynamics written in the form

$$D(q)\ddot{q} + C(q, \dot{q})\dot{q} + G(q) = Bu + J^T F_{\text{ext}} \quad (3.16)$$

where D is the mass matrix, C contains the Coriolis and centrifugal terms, G is the vector of forces which are gravity dependent, and B is the mapping of the input vector u to the generalized coordinates. Additionally, J is the contact Jacobian which is used to model and ensure the foot does not slip, and F_{ext} is the interaction force with the environment, and is zero when the leg is in flight.

To model the contact between the toe and the ground, a Coulomb friction model is implemented, which results in

$$J^y \ddot{q} + \dot{J}^y \dot{q} = 0 \quad (3.17)$$

$$J^x \ddot{q} + \dot{J}^x \dot{q} = 0 \quad \text{or} \quad F_{\text{ext}}^x = \mu F_{\text{ext}}^y \quad (3.18)$$

and is used in (3.16) to solve for \ddot{q} and F_{ext} . The friction coefficient μ accounts for any occurrence of potential sliding; in which case the constraint is enforced.

The model is a hybrid dynamical system consisting of both a flow for the flight phase and stance phase, respectively. Switching between the two intuitively occurs when the foot touches down with the ground, or lifts off the ground. The stance dynamics consist of a reduced-order system

$$D_{\text{st}}(q_{\text{st}})\ddot{q}_{\text{st}} + C_{\text{st}}(q_{\text{st}}, \dot{q}_{\text{st}})\dot{q}_{\text{st}} + G_{\text{st}}(q_{\text{st}}) = B_{\text{st}}u \quad (3.19)$$

where the subscript st denotes the stance phase. The configuration variables are $q_{\text{st}} := (\theta_1, \theta_2)$. This is due to the dimension reduction of the configuration variables.

In the stance phase, the x and y coordinates of the boom's COM can be solved by the trigonometry of the hip and knee angles

$$y = L_1 \cos(\theta_1) + L_2 \cos(\theta_2 - \theta_1) \quad (3.20)$$

$$x = L_2 \sin(\theta_2 - \theta_1) - L_1 \sin(\theta_1) \quad (3.21)$$

where L_1 and L_2 are the lengths of the thigh and shank, respectively, and θ_1 and θ_2 are the hip and knee joint angles, respectively.

The input, u , to the system described in both (3.16) and (3.19) reflect not only the control input, but also account for external forces such as the spring and friction.

$$u = \tau_{\text{active}} + \tau_{\text{spring}} + \tau_{\text{damping}} \quad (3.22)$$

with,

$$\tau_{\text{active}} = \tau_{\text{Hip}} + \tau_{\text{Knee}} \quad (3.23)$$

$$\tau_{\text{spring}} = k_{\text{Rot}}(\theta_2 - \theta_2^{\text{td}}) \quad (3.24)$$

$$\tau_{\text{damping}} = -b\dot{\theta}_2 \quad (3.25)$$

where τ_{Hip} and τ_{Knee} are the torques from the motors at the output of the gearbox shafts, which are applied at the hip and knee joints, respectively. k_{Rot} is the rotational stiffness shown in Fig. 3.2, from the passive spring, with θ_2^{td} being the knee angle at touchdown. Lastly, b is the lumped damping coefficient which represents the kinetic friction forces applied at the knee joint. Note that during flight phase the spring does not contribute to the dynamics of the flight phase, and therefore is zero in (3.22) during flight. Additionally, since the model assumes friction is negligible, u_{damping} does not participate in (3.22) when the leg is in flight.

Chapter 4

ANALYSIS AND EVALUATION OF SPEAR-II

This chapter will discuss the analysis of the design of SPEAR-II based on the model derived in the previous chapter. Our objective is to better understand the interactions between the passive spring element of the Sw-PEA, and the motor. The discussion starts with parameter identification experiments which provides the data necessary to assess the model's validity as well as estimate unknown values of the its parameters. By capturing insights from these experiments, the model is updated to more accurately reflect the physical robot, and is used in the controller design and simulation to fine-tune the control variables. The chapter concludes with hopping-in-place experiments using SPEAR-II.

4.1 Parameter Identification Experiments

4.1.1 Motivation

The objective of estimation, and the parameter identification experiments is twofold: the estimate important parameters of the model, and to assess how energy flows in the system. To better understand the interactions occurring internally in the robot, an experiment is proposed to isolate and quantify the behavior of the knee motor and transmission system. The objectives of the parameter identification experiments and analysis are the following:

- Estimate k_{Rot} , and b to refine the SPEAR-II model
- Understand the dynamic effects of gearbox and motor selection
- Understand the energetic effects of backdriving the knee motor

In more detail, parameters in the model shown in Section 3.3 are estimated. This includes the lumped rotational stiffness at the knee joint, k_{Rot} , and the coefficient b used to model friction in the system. It is assumed that the timing belt transmission system will add a spring force that is in parallel with the spring S_1 , which will increase the overall lumped rotational stiffness k_{Rot} at the knee joint. The mechanical components involved in actuating the shank is also assumed to add friction due to the gearbox, belt, rotating components in the motor, and potentially back-emf effects. This is represented in the model as a Coloumb damping force with a coefficient, b , however, the numerical value of this parameter is hard to derive or guess a priori. The value of b is estimated using the model and experimental data in the same manner as k_{Rot} .

After estimating the parameters of the model, the influence of the gearbox selection on the system is simulated using the refined model. The model is re-derived for each simulated configuration with different gearbox ratios. The intuition is that the inertia of the system will be altered by the change in gearbox configuration due to reflected rotor inertia being proportionate to the square of the gear ratio, that is $J_{\text{reflected}} = N^2 J_{\text{rotor}}$. The motivation of this analysis is to understand the effect of selecting a different knee motor or gearbox than the current one on SPEAR-II, should a new motor be required in the future.

Lastly, the motivation of understanding the energetic effects of the knee actuator being engaged and in parallel to the spring at the knee joint. Previously, an understanding of the energy flow for SPEAR-I is found in [27], and accounts for the energy flow from the battery through the motors and mechanical components of the system. This is represented in Fig. 4.1 where the desired energy flow is captured by the green arrows, and the energy losses are captured by the red arrows.

While Fig. 4.1 captures the important routes of energy flow in typical use of the SPEAR leg design, there are additional possible energy transfers from external forces driving the motor shaft. Recall that the knee joint couples both the motor and the spring. The knee joint motion backdrives the transmission of the actuator and rotates the rotor of the motor. This potentially implies that part of the energy that would go

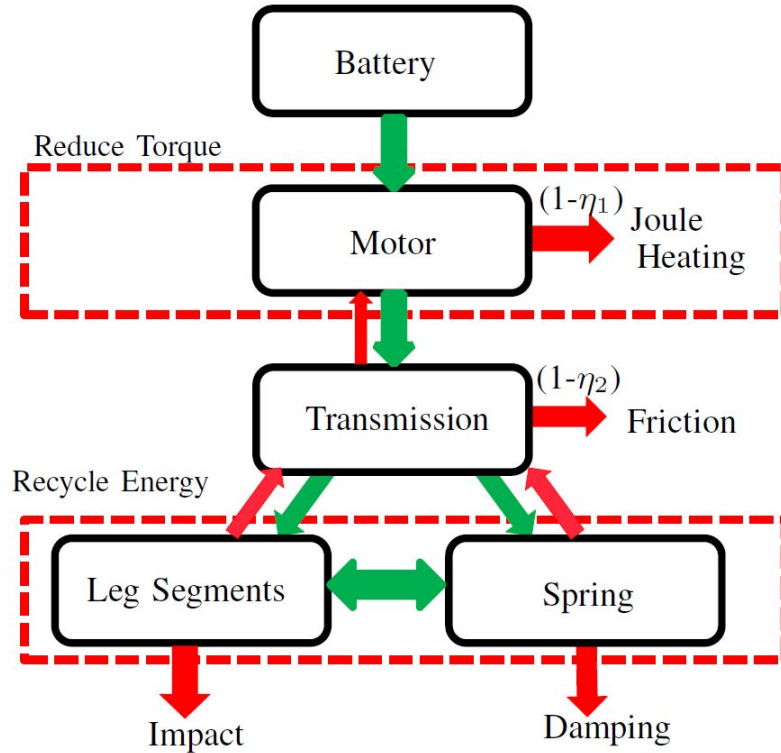


Figure 4.1: Energy flow diagram of SPEAR-I; see [27]

into the spring to be used for locomotion could be wasted by losses associated with backdriving the motor. The known energy losses are accounted for by the following:

- Joint Friction
- Bearings
- Gearbox Friction
- Belt Deformation
- Potential Back-emf

To quantify this, it is important to estimate the lumped knee stiffness k_{Rot} , and friction term coefficient b through the parameter identification experiments. An experiment is proposed to fulfill these objectives and understand the interactions relating to the motor being engaged to the knee joint, and in parallel with the spring.

4.1.2 Experiment Model

Consider the model of the experiment in Fig. 4.2. When the leg is in stance, it is assumed that there is no slip between the toe and the ground. With the toe, knee and hip joint considered as revolute joints, the mechanism can be viewed as a variation to the crank-slider mechanism, where the boom assembly is the slider, and the shank is the input link.

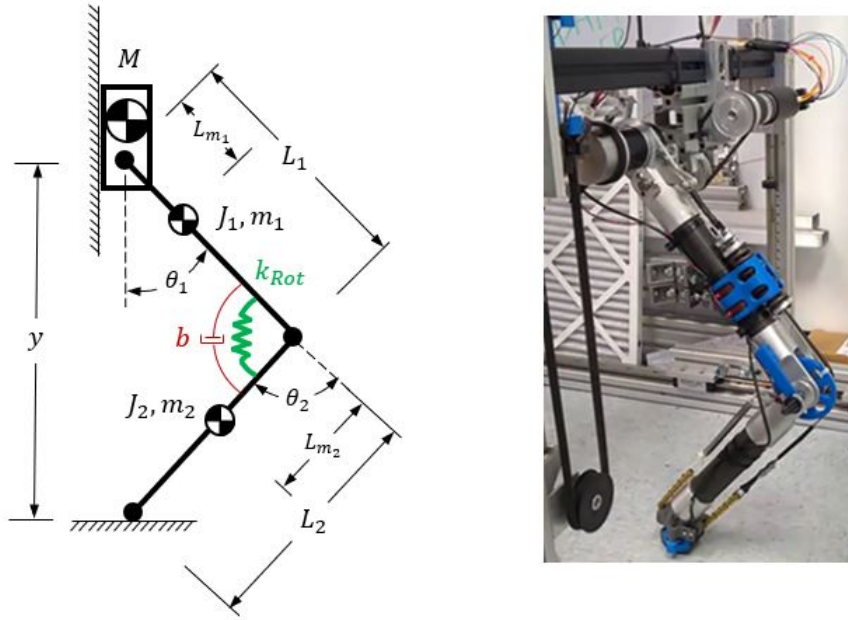


Figure 4.2: Model of the SPEAR-II leg in stance phase and the side view of the leg to compare during a parameter identification experiment.

Due to the geometric constraints of the leg in the configuration shown in Fig. 4.2, it can be observed that the system can be described by one of the joint angles, θ_1 or θ_2 . Since the focus of the experiment is on the measurement of the knee angle θ_2 , and $x_{hip} = 0$ (by constraint), θ_1 and $\dot{\theta}_1$ are represented as functions of the knee angle θ_2 . Additionally, the height of the boom y , and its velocity \dot{y} , are similarly represented as functions of the knee angle θ_2 , i.e.

$$\theta_1 = \arctan\left(\frac{L_2 \sin(\theta_2)}{L_1 + L_2 \cos(\theta_2)}\right) \quad (4.1)$$

$$y = L_1 \cos(\theta_1) + L_2 \cos(\theta_2 - \theta_1) \quad (4.2)$$

By substituting (4.1) into (4.2), the following variables can also be expressed completely as functions of θ_2 :

$$\dot{\theta}_1 = \frac{L_2 \dot{\theta}_2 \cos(\theta_2 - \theta_1)}{L_1 \cos(\theta_1) + L_2 \cos(\theta_2 - \theta_1)} \quad (4.3)$$

$$\dot{y} = -L_1 \dot{\theta}_1 \sin(\theta_1) - L_2 (\dot{\theta}_2 - \dot{\theta}_1) \sin(\theta_2 - \theta_1) \quad (4.4)$$

With the simplifications of the geometric constraints, the complexity of the model is reduced with the configuration variables being only θ_2 and $\dot{\theta}_2$. The dynamics model for the push test experiment follows the same procedure as shown in Section 3.3 with the following differences:

- Experimental constraints: $x_{\text{hip}} = 0$, and hence $\dot{x}_{\text{hip}} = 0$, and toe fixed to ground as revolute joint.
- For the experiments when the knee motor is disconnected from the joint, the rotors inertia is zero and is absent from the model.
- The damping of the knee joint results in the torque $u_{\text{knee,damping}} = -b\dot{\theta}_2$ where b is the damping coefficient.
- No torque will be applied from the motors to either of the joints; hence, for both joints, $u_{\text{active}} = 0$.

4.1.3 Procedure of Experiment

A simple experiment was designed using the SPEAR-II leg to collect data to evaluate the effect of the added inertia of the knee motor assembly term. The experiment involves setting the leg at a rest as shown in 4.2 and applying a force, F_{Push} , to lower the height of the hip joint (and the boom), by three prescribed amounts: -5cm , -7.5cm , -10cm . This force increases the angle of the knee joint from the rest angle, and in effect deforms the spring S_1 to create torque at the knee joint.

This experiment is repeated for two different experiment types, corresponding to two different arrangements of SPEAR-II:

1. Motor Engaged
2. Motor Not Engaged (by removing timing belt)

The outline of the experiment is shown in Fig. 4.3. The diagram on the left shows the configuration of the system prior to the start of the experiment. The boom is held down at a height of Δy by a static force F_{Push} , which compresses the spring at the knee and creates a torque at the knee shown as τ_{spring} in the figure. At the start of the experiment the force F_{Push} is instantly released, and the torque τ_{spring} moves the system until the potential energy in the spring is fully dissipated.

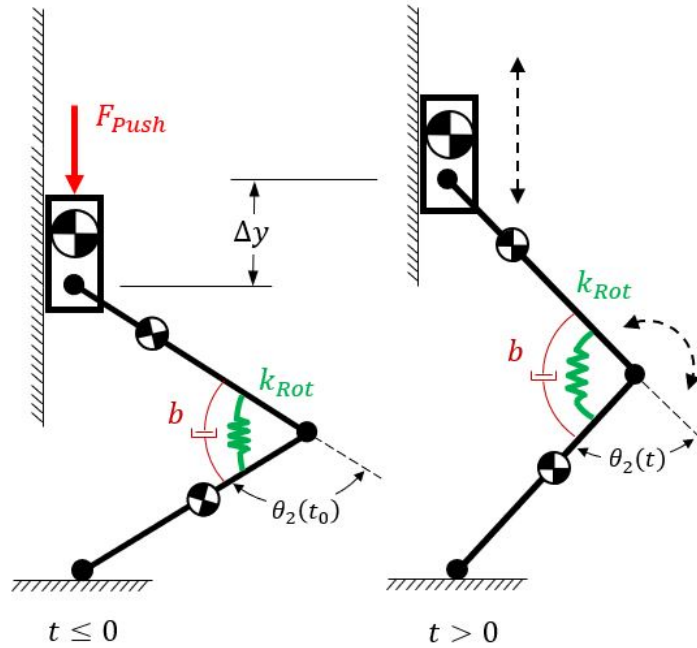


Figure 4.3: Schematic of the SPEAR-II Leg during the push experiment.

After the leg is depressed to a static equilibrium at Δy , the force, F_{Push} , is released instantaneously at time $t = 0$ and allows the stored spring energy in the knee

joint to be released into the system. This experiment is repeated 5 times for each of the three Δy values. First, these three sets of experiments are conducted in the standard setup of the leg, with the knee motor engaged to the joint via the timing belt transmission mechanism. Following the sets with the motor engaged, the timing belt is removed to disengage the knee motor from the joint.

To summarize the experiment procedure:

1. Slowly push boom to specified height using graduated measurement markings on boom.
2. Hold the boom at the specified height so the system starts at a static equilibrium.
3. After 3 seconds, instantly release the boom without any interference.
4. Once the leg comes to rest for 3 more seconds, repeat the procedure, as desired.

The knee angle is measured by using the potentiometer located at the knee joint. This provides a consistent, direct measurement for both scenarios when the motor is engaged and disengaged. The voltage reading of the potentiometer is measured by the analog input of the communications board on the PC-104 stack of the robot shown in Sec. 2.4.5. The voltage taper is linear for the potentiometer, and creates a linear relationship between the angle of the joint and the measured voltage. The slope of the function is known a priori to the experiment, and was obtained as part of the calibration of SPEAR-II after assembling the robot.

The approach for processing the raw voltage data of the potentiometer is consistent for all data sets of the Parameter Identification experiments, and is executed with a series of MATLAB[®] scripts. First, the data is smoothed by filtering with a moving average of the 100 data point window (note that the measurements are sampled at 1000Hz). After the data is filtered, the voltage is converted to joint angle data in radians using the known linear relation. The filtered and converted data is then used by the greybox estimation toolbox for parameter identification.

More specifically, the procedure for processing the data and estimating the model parameters is conducted by the following:

1. The raw voltage data of the knee potentiometer is converted to angle measurement (in radians) using the linear relationship between the two.
2. Since the signal is noisy (due to the voltage measurement), the newly converted angle measurement is smoothed using a moving average filter with a window size of 100 data points.
3. The experiments are classified by their initial conditions, Δy , and their experiment type, either with or without the motor connected.
4. Depending on the experiment type, use the correct model to account for the rotor inertia as part of the system or not. The unknown parameters are k_{Rot} and b .
5. The model is matched with the experiment measurement of the knee angle (from step 2), and is the output of the model for the estimation procedure. The corresponding initial conditions from the experiment are inputs to the model.
6. Using the `nlgreyest` package in MATLAB[®], the unknown parameters are estimated using a nonlinear least squares solver to minimize the mean squared error (MSE) of the model output with the estimated parameters. This is repeated by the algorithm until the solver finds the best fit.
7. Repeat steps 5 and 6 until estimated parameters are found for all three experiment initial conditions, and both conditions (with and without motor).

4.1.4 Results and Analysis

The results of the parameter identification experiments are tabulated and displayed in Table 4.1. Each of the estimated parameters are k_{Rot} , the lumped rotational stiffness value, b , the lumped damping coefficient to model the various friction forces, and RA , the resting angle of the knee joint. The σ parameters in the table represent the standard deviation of the estimated parameters for the corresponding subscripts. Lastly, $\%Fit$ is the percentage to which the model fits the experimental data with the estimated parameters for the corresponding set. Note that the values for k_{Rot} are in $\frac{Nm}{rad}$, b are in $\frac{Nm}{rads^{-1}}$, and RA are in rad .

Table 4.2 shows a tabulation of the average of the estimated parameters shown in Table 4.1 for both the case with the motor, and without the motor. The average of these values provide insights into the distinctions between the two cases. Two specific parameters than have observable differences are k_{Rot} , and b . The difference in k_{Rot} is

Table 4.1: Tabulation of the estimated model parameters using MATLAB[®] System Identification Toolbox.

| Exp. Type | k_{Rot} | b | RA | $\sigma_{k_{Rot}}$ | σ_b | σ_{RA} | %Fit |
|------------------|-----------|------|------|--------------------|------------|---------------|-------------|
| With Motor 5cm | 49.88 | 1.56 | 1.01 | 9.97 | 0.81 | 0.05 | 86.30% |
| With Motor 7.5cm | 55.93 | 1.35 | 1.03 | 6.3 | 0.47 | 0.03 | 88.20% |
| With Motor 10cm | 48.25 | 1.03 | 1 | 2.97 | 0.23 | 0.02 | 84.10% |
| No Motor 5cm | 48.31 | 1.3 | 1 | 8.74 | 0.66 | 0.05 | 90.30% |
| No Motor 7.5cm | 48.53 | 1.02 | 1 | 5.08 | 0.37 | 0.03 | 89.60% |
| No Motor 10cm | 47.12 | 0.8 | 1 | 2.59 | 0.19 | 0.02 | 83.00% |

an increase in $0.85 \frac{Nm}{rad}$, and an increase of $0.26 \frac{Nm}{rads^{-1}}$ for b . This indicates increased friction and stiffness due to the transmission mechanism and motor assembly.

Table 4.2: Tabulation of the average estimated model parameters using MATLAB[®] System Identification Toolbox.

| Exp. Type | k_{Rot} | b | RA | $\sigma_{k_{Rot}}$ | σ_b | σ_{RA} | %Fit |
|--------------------|-----------|------|------|--------------------|------------|---------------|-------------|
| With Motor Average | 48.84 | 1.3 | 1 | 6.19 | 0.5 | 0.03 | 84.62% |
| No Motor Average | 47.99 | 1.04 | 1 | 5.47 | 0.41 | 0.03 | 87.62% |

The model has shown to provide effective accuracy when implementing the System Identification Toolbox in MATLAB[®]. The procedure for estimating parameters involves first building the nonlinear model derived earlier in this section, and specifying the parameters to be estimated: in this case, k_{Rot} , b , and RA , with the spring and damping forces treated as parameters of the dynamics model. Comparisons between the model with estimated parameters from Table 4.1, and the experimental data sets are shown in Fig. 4.4. The six plots show the knee angle versus time. The plots on the left side are the experiments with the motor, and the plots on the right side are the experiments without the motor. Each row is for the varying initial conditions of Δy with the top row being 5cm, the middle row 7.5cm, and the bottom row 10cm. The grey lines are the experimental data sets, where as the red line shown in each is the model with the estimated parameters to display the model fit.

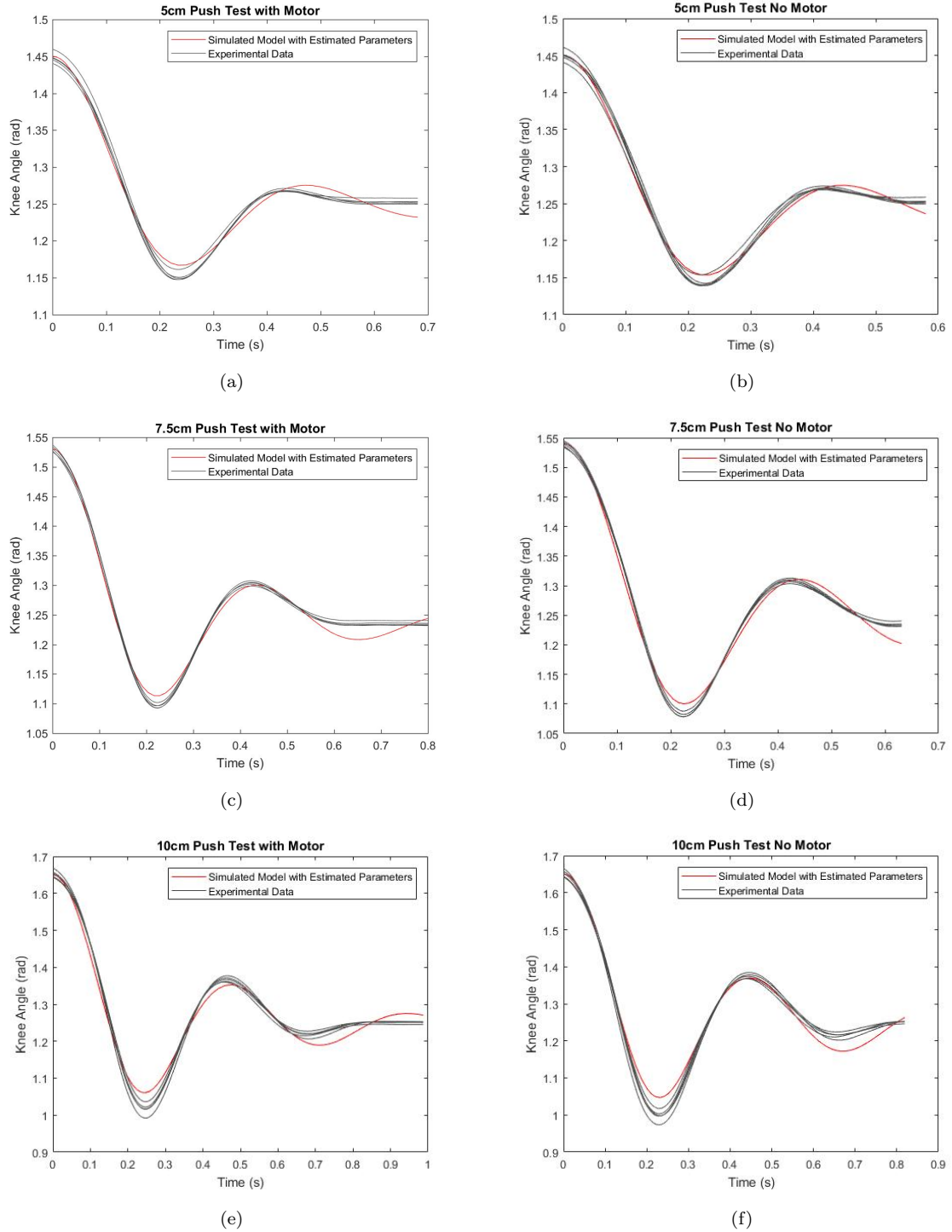


Figure 4.4: The 6 different sets of experiments. Figures (a), (c), and (e) are all done with the motor engaged at the knee joint. Figures (b), (d), and (f) are conducted with the motor disengaged from the knee joint.

4.1.5 Discussion and Summary

4.1.5.1 Increased Stiffness and Friction with Motor

Notice the differences between the motor and no motor case shown in the table of the averages of the estimated spring stiffness values and damping coefficient. The distinct difference in the rotational spring stiffness k_{Rot} for the two cases can be attributed to the torque transmission mechanism. The fiber-reinforced neoprene timing belt has a springy behavior when engaged. More specifically, the neoprene material in the belt acts as a soft rotational spring in parallel with the Sw-PEA hard spring, S_1 . The theoretical stiffness can be estimated by calculating the deformation of the belt using the model configuration, and the material properties provided by the timing belt manufacturer. The predicted stiffness added by the transmission mechanism lines-up closely with the estimated difference.

The spring force of a deformed linear elastic material yields a formula that is essentially Hooke's Law

$$F_{\text{Belt}} = \frac{EA}{L_0} \Delta L \quad (4.5)$$

where E is the Young's Modulus of the material, A is the cross-sectional area, L_0 is the undeformed length, and ΔL is the deformation of the belt. With the force acting along the direction of the timing belt, as a moment couple about the knee joint, the effective moment can be expressed as a rotational spring.

$$M_{\text{Belt}} = \frac{2EA}{L_0} r^2 \Delta \theta \quad (4.6)$$

or, equivalently,

$$M_{\text{Belt}} = k_{\text{rotBelt}} \Delta \theta \quad (4.7)$$

Using the values for SPEAR-II and the timing belt, the modulus of Neoprene ranges from $E \in [13.8, 20.7] \text{MPa}$, $L_0 = 0.3048 \text{m}$, $A = 1.242 \text{m}^{-5}$, and $r = 0.0254 \text{m}$. With the

given values, we obtain a theoretical range of $k_{\text{rotbelt}} \in [0.73, 1.09] \frac{Nm}{rad}$, which lines-up closely with the difference of the estimated averages shown in Table 4.2 , $0.85 \frac{Nm}{rad}$

Additionally, a noticeable parameter difference between the motor and no motor case is the damping coefficient, which models the frictional forces affecting the knee joint. There is an increase in damping which is attributed to the added Coulomb friction from the belt transmission system and the planetary gearbox, as well as miniscule amounts of electrical dissipation due to eddy currents and magnetic resistance in the motor assembly.

4.1.5.2 Gearbox Effect on Dynamics

Fig. 4.5 overlays the 10cm initial condition experiments for both the motor and no motor cases. Both plots show the knee angle versus time. The plot on the left shows the experiment data for the motor and no motor cases. The plot on the right shows the model of each case simulated with the estimated parameters for the corresponding case.

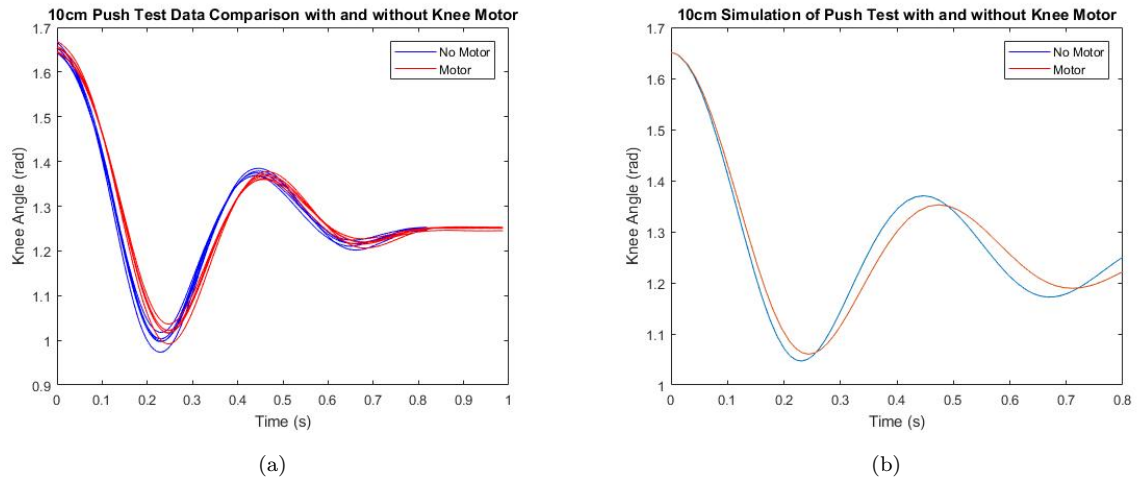


Figure 4.5: Plots comparing the model with experimental data, and simulation of corresponding models.

Notice the difference of the added reflected inertia from the motor and gearbox can be observed by the lag in frequency in the red line versus the blue line. The added

rotational inertia effectively changes the natural frequency of the system, and shows there is a noticeable effect on the dynamics that is influenced by the motor and gearbox selection.

The effect of the rotor inertia by the lag is shown in Fig. 4.5 for both the simulation and experiment where the peak of the red lines occur later than the peaks of the blue lines. The total rotational inertia of the system is increased because the rotor inertia is amplified by the gearbox, and has an impact on the properties of the overall leg motion. As seen by the comparison of the data shown in Fig. 4.5 between having the knee motor engaged or disengaged, there is a clear lag and change in natural frequency of the system, caused by added inertia term from the motor and gearbox.

The Parameter Identification Experiment shows that there are changes to the system dynamics that are influenced by the gear ratio and motor selection in the Sw-PEA. These design inputs can have noticeable impacts on the dynamics of the system. The effect of the reflect rotor inertia (felt at the joint), which was previously unconsidered and unaccounted for, can have a significant effect on the motion of a leg using the Sw-PEA. To further investigate the influence of the gearbox on the reflected inertia, and overall rotational inertia of the system, the experiment model of SPEAR-II is simulated for the same experiment but with varying gearbox ratios.

The effect of varying gearbox ratio for the experiment is simulated and shown in Fig. 4.6. The plot shows the knee angle of the robot versus time for the duration of the simulation. The purple line is the simulation output for the model of the no motor case with the estimated parameters from the experiment. The blue line is the model of the SPEAR-II with the motor engaged, and the estimated parameters from the experiment. The red line represents a model of the system with the knee motor gear ratio increase from 15:1 to 30:1, where the dynamics are derived to account for the reflected rotor inertia. Lastly, the yellow line represents a model of the leg with a 66:1 gear ratio, where the dynamics model is derive to account for the reflected rotor inertia. Note that 30:1, and 66:1, are off-the-shelf planetary gears that are available and compatible with the Maxon[®] knee motor on SPEAR-II, to show the effect of using

a different gearbox with the same motor.

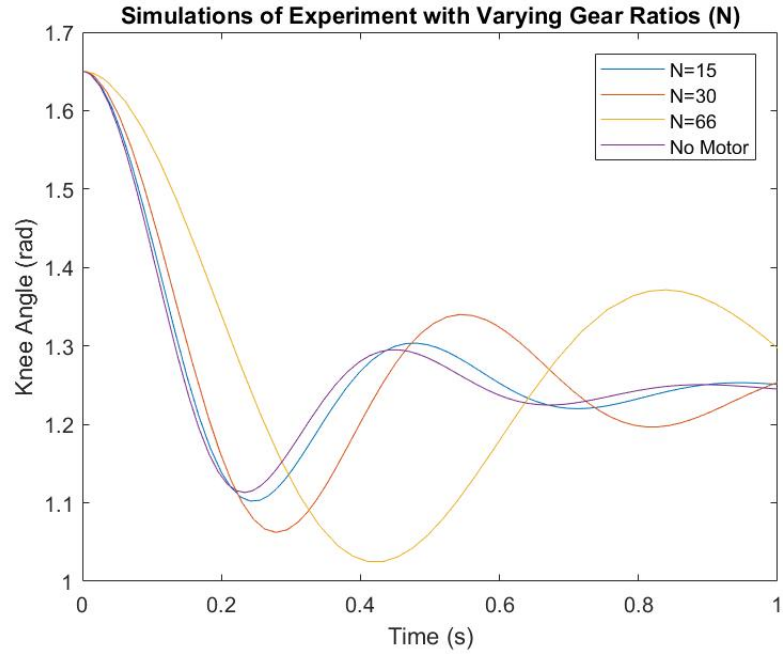


Figure 4.6: Simulation of the 10cm experiment varying gear ratios for SPEAR-II.

Notice the variation in the response of the system due to the increase of gear ratio. The change in the natural frequency of the system is observed by the visible lag in the responses. This is caused by the large increase in the reflected rotor inertia which is proportionate to the square of the gear ratio, N^2 . Gradually, the reflected inertia dominates the inertia term of the system dynamics. This illustrates an important design concept for legged robots, especially designs using Sw-PEAs, which is that selection of the motor and gearbox can have an observable effect on the system. Overall, it is best to maintain a smaller gear ratio in the design.

The results from the simulation, shown in Fig. 4.6, account for the estimated change in damping ratio, as well as the added rotational inertia. As the gear ratio increases, the effective rotor inertia dominates the total inertia term increases. This implies that the energy transferred from the spring is likely used primarily for the

kinetic energy of the rotor. This factor could potentially have further implications on energy efficiency due to the added losses both mechanical, and possibly electrical.

4.1.5.3 Negligible Electromechanical Interactions

An area of interest of the parameter identification experiments, is to better understand the interaction between the spring and motor in the context of energy flow and transfer. The Sw-PEA mechanism was design from the perspective of having the motor drive the spring when added spring compression is needed. However, a scenario could occur where the spring could backdrive the motor while they are engaged in parallel. This situation would be a case where the spring could transfer power to the motor which would now be acting as a DC electric generator. With energy efficiency in mind for the SPEAR-II concept and design, a more in-depth understand of this interaction is desired, and is investigated with parameter identification experiment results.

To test the potential generator effect of backdriving the motor, a variation of the parameter identification experiment is conducted. A similar set of data is obtained with the same conditions as the *withmotor* case, however, the only change is that the circuitry which provides the motor power is now connected; creating an electrical load on the potential DC generator. Fig. 4.7 highlights the result of this experiment by comparing the relative height of the boom versus time for each of the three cases. The blue lines represent the data for the case which the timing belt is removed and the motor is decoupled from the knee joint. The red lines are the results for the case where the motor is engaged to the knee joint, but the power that normally supplies the motor is disconnected. The green lines represent the results of the third case where the motor is engaged and the circuitry that supplies power to the motor is connected.

Note that in all cases, there is no current commanded and hence the motor is passively attached to the knee joint whenever it is engaged (but does not provide any torque). A key takeaway from the results in Fig. 4.7 is that there is an indistinguishable difference between the case with the power connected and disconnected. This implies

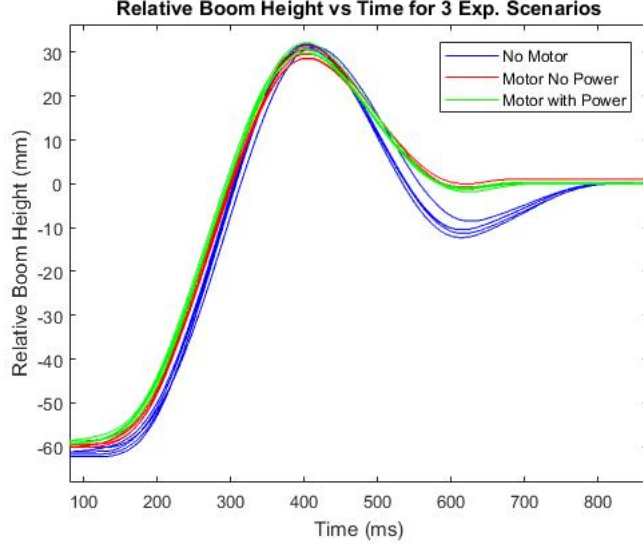


Figure 4.7: Experimental results illustrating the effect of the PWM amplifiers H bridge allowing the motor to rotate without additional resistance, as a no-load generator.

that the motor does not lose much energy due to dissipation of electrical current (which would be generated by the motor), which can be explained by the H bridge circuitry in the PWM amplifiers for the motors.

In previous work regarding the Sw-PEA and the first iteration of SPEAR, the interactions between the electromechanical components were modeled as a standard torque-current relationship $\tau = k_{\tau}i(t)$, where τ is the motor torque, $i(t)$ is the applied current, and k_{τ} is the specific motor constant. While this is correct, it could potentially lead to overlooked phenomena occurring internally. This has the potential to alter the understanding of energy transfer between components of the Sw-PEA architecture, as well as efficiency calculations, due to the coupling of the parallel compliant element and the actuator itself.

During the stance phase of hopping, the knee motor and spring are inherently connected to each other. The spring is intended work with the system to improve energy efficiency by absorbing energy during the compression portion of stance, and recycling it for liftoff. However, it could be possible for the spring to translate some

of the stored mechanical energy into electrical energy. This is the potentially the case when the leg is in stance and the compressed spring drives the rotor externally through the couple of the motor and knee joint. In this scenario, the knee motor can be modeled as a DC generator. The mechanical power from the spring S_1 could flow through the shaft of the gearbox and motor and creating electrical power by rotating the DC motor's permanent magnets across the coils in the housing. This effect could not only influence energy efficiency, but can additionally affect the motion by potentially creating added friction forces internally at the motor and PWM circuitry, by inducing currents and eddy currents which are dissipated and can even produce magnetic resistance to motion. These effects are assumed to be small, but there is interest in understanding the interactions occurring from backdriving the motor.

As discussed in Section 2.4.5, the Maxon knee motor is powered by a PWM (pulse width modulation) amplifier utilizing a 24V battery. Internally, there is sophisticated circuitry that can control the direction of the motor, as well as enable braking and coasting of the motor. As an example, consider the simple H bridge shown in Fig. 4.8. The circuit is designed such that depending on the switch configuration, the motor will behave differently. With reference to Fig. 4.8, when switches S_1 and S_4 are closed, while the others are open, the motor will rotate in the clockwise direction, with the direction of the current flowing from the left-side of the motor, through to the right-side. Additionally, in an opposite configuration, where switches S_3 and S_2 are closed while the others are open, the motor will rotate in the opposite (counter-clockwise) direction. Lastly, while there are numerous other configurations of the four switches, one important configuration is where the motor can coast. This is the case when all four switches are open, and in which case the motor would behave as a no-load generator.

With the concept of an H bridge circuit described, the extension of the circuit's structure for a 3-phase BLDC (brushless DC) motor is intuitive. Shown in Fig. 4.9, is the model of the circuit used for SPEAR-II. In the case of SPEAR-II, the PWM amplifier operates in a very similar fashion where the switches enable current between

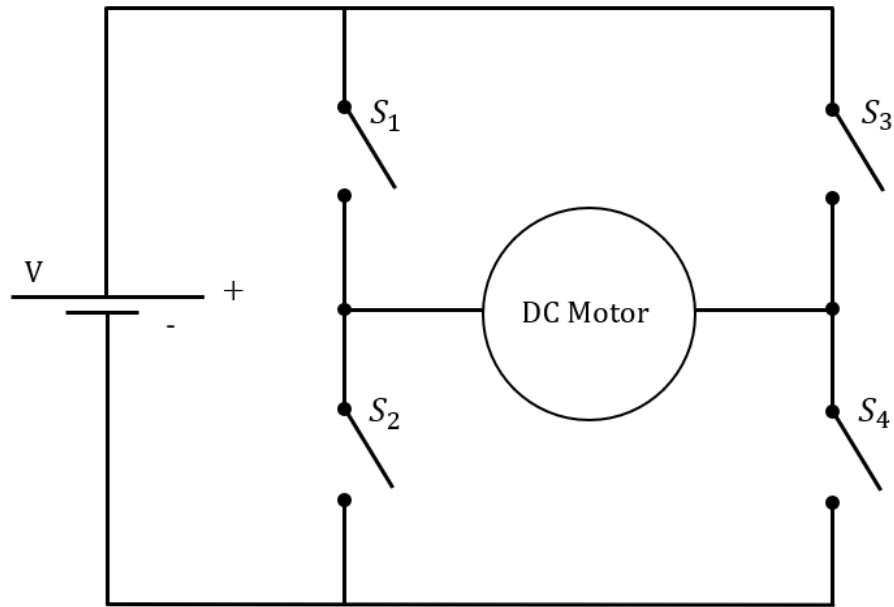


Figure 4.8: Simple circuit diagram of a basic H Bridge setup used in a conceptual motor control application. By changing the switches, the flow of current can control the direction of the motor, as well as braking and coasting.

specific phases to rotate the motor in a desired direction with a desired current. One important fact to note, is that when zero current is commanded from the controller, the motor has zero electrical load due to the switches of the H bridge being all open. From a modeling perspective, this means that the motor does not convert mechanical power to electrical power while this configuration is in place, and therefore should result in negligible added frictional forces due to back emf.

Although this is not the case in our experiments, the electronic configuration of SPEAR-II can generate electrical power from mechanical interactions at the joint only when the direction of the current and the external torque are opposites. For example, when the H bridge is configured to generate clockwise motion of the motor, and an external applied torque drives the motor shaft in a opposite direction, there is electrical power generated due to the load of the circuit. If the voltage generated by

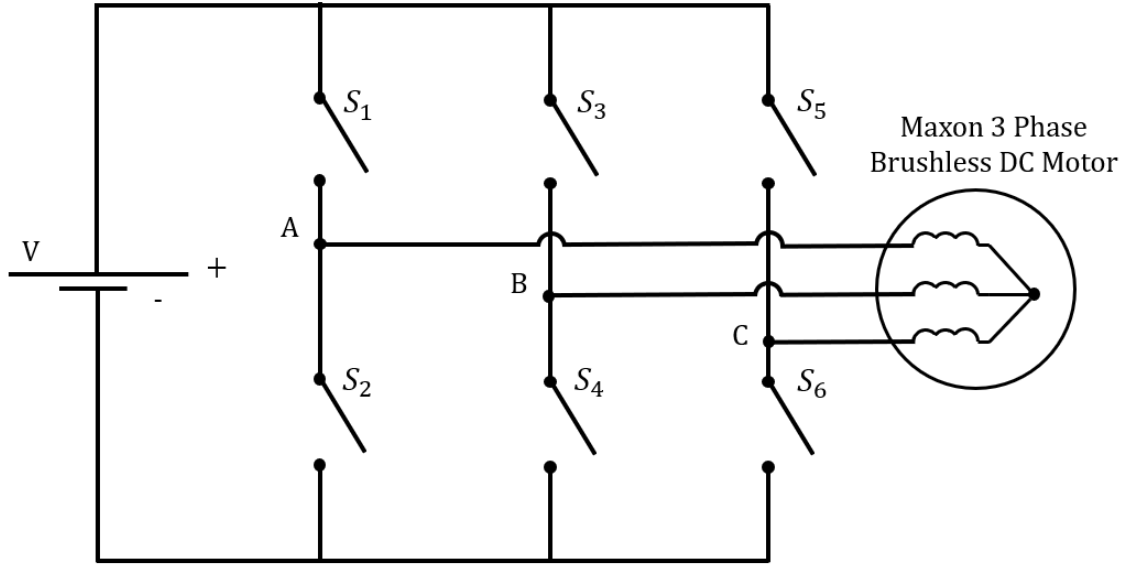


Figure 4.9: Model of the H bridge circuit used in the PWM amplifier for the Maxon (knee) motor in SPEAR-II. The structure is similar to the simple H bridge example shown in Fig. 4.8 but is expanded for the capability of handling the 3 motor phases of the brushless DC (BLDC) Motor.

the rotation of the motor is larger than the battery, and it induces a current (opposite to the applied current), then the battery can be recharged by the conversion of the externally applied mechanical power at the shaft. In practice, the Sw-PEA actuator is designed in conjunction with the controller of the leg to be synergistic. Hence, the generative effect described typically does not occur often. However, with the analysis shown of the interactions at the electromechanical level, the modeling framework can consider these scenarios, and enables a designer of an Sw-PEA robot or controller to be cognizant of these effects.

As a final comment, note that the voltage generated by spinning the rotor externally is:

$$V_{bemf} = -K_v \dot{\theta}_{\text{rotor}} = -K_v N \dot{\theta}_{\text{joint}} \quad (4.8)$$

Specifically for SPEAR-II, the knee motor parameters are $N = 15$, $K_v = 0.115 \frac{V}{\text{rad-s}^{-1}}$. As a quick example calculation, this implies that the voltage generated by the rotor spinning at $20 \frac{\text{rad}}{\text{s}}$ is $34.5V$. Angular speeds for a rotor such as this occur as peak velocities during hopping experiments and can be observed in measurement of the current, if the voltage has a load on the circuit, and is connected via the H bridge circuit. Furthermore, for the chosen knee motor on SPEAR-II, a change in gear ratio can influence the damping coefficient of the knee joint. This illustrates the effect of the design decision of gear ratio selection for the knee motor, and the resulting impact on the energy efficiency of leg. Note that the both the voltage and the potential power generated are functions of the gear ratio.

4.2 Controller Tuning and Simulation

Using the model for SPEAR-II shown in Section 3.3, and combining the estimated parameters found in the previous section. We now discuss the implementation of a controller for hopping in both experiments and simulations.

4.2.1 Controller for Hopping-in-Place

The controller for hopping-in-place is designed with two objectives in mind. First, during flight the goal is to control the joint angles of the leg. Second, during stance the goal is to allow the spring to do most of the work in stance phase while injecting some added energy to make up for damping losses.

In more detail, during flight phase, the hip and knee angles are commanded with a simple PD control, as follows,

$$\tau_{\text{hip}} = \begin{cases} K_{\text{hip}}(\theta_{\text{hip}} - \theta_{\text{hip}}^{\text{des}}) + K_{D_{\text{hip}}}\dot{\theta}_{\text{hip}}, & \text{if } y_{\text{toe}} > 0 \\ \bar{\tau}_{\text{hip}}, & \text{if } y_{\text{toe}} = 0 \end{cases} \quad (4.9)$$

where K_{hip} is the proportional gain of the controller, and $K_{D_{\text{hip}}}$ is the derivative gain of the controller. $\theta_{\text{hip}}^{\text{des}}$ is the desired touchdown angle of the hip, θ_{hip} is the hip angle, and $\dot{\theta}_{\text{hip}}$ is the angular velocity of the hip. $\bar{\tau}_{\text{hip}}$ is a nominal torque that is sometimes

applied at the hip to help maintain contact with the ground. The nominal torque is typically very small and can be considered negligible.

The gains for each are tuned from classical PD tuning techniques, with the objective of reaching the desired angle before touchdown, with nearly zero angular velocity.

During stance, the torque of the hip motor is commanded to be zero while the knee motor is driven to work with the passive spring, and inject energy into the spring, as well as push off the ground to enter flight phase. This is done by applying a negative torque during the first half of the stance phase and then applying a positive torque during the second half of the stance phase. The duration of the stance phase is first computed in simulation, and is updated from experimental data to more accurately match the motion of the leg. Mathematically, the stance controller is,

$$\tau_{\text{knee}} = \begin{cases} K_{\text{knee}}(\theta_{\text{knee}} - \theta_{\text{knee}}^{\text{des}}) + K_{D_{\text{knee}}} \dot{\theta}_{\text{knee}}, & \text{if } y_{\text{toe}} > 0 \\ -\bar{\tau}_{\text{knee}} \text{sign}(\sin(2\pi f(t - t_{\text{td}}))), & \text{if } y_{\text{toe}} = 0 \end{cases} \quad (4.10)$$

where K_{knee} is the proportional gains of the controller, $K_{D_{\text{knee}}}$ is the derivative gains of the controller, f is the frequency of the hopping cycle during stance phase, and t_{td} is the touchdown time at which the toe comes into contact with the ground. $\theta_{\text{knee}}^{\text{des}}$ is the desired touchdown angle for the knee, θ_{knee} is the knee angle, and $\dot{\theta}_{\text{knee}}$ is the angular velocity of the knee. $\bar{\tau}_{\text{knee}}$ is the magnitude of the torque profile during stance, which changes signs depending on the time after the touchdown event.

4.2.2 Simulation and Tuning of Control Parameters

Using the controller structure described above in conjunction with the model of SPEAR-II and the estimated parameters, the remaining controller tuning parameters are calculated using simulation of the monopodal model. The important control parameters of interest are the K_P and K_D gains for both motors, as well as the hopping frequency f in (4.10), and the touchdown angles of the knee and hip. If the frequency term is not sufficiently accurate during hopping, the actuator will work opposite of

the passive spring element, and the natural limit cycle behavior of the robot's hopping motion will be out of sync in practice.

The hopping-in-place gait for SPEAR-II is modeled through a Poincaré return map with the stance phase and flight phase being the continuous-time phases, and the switching surfaces between them corresponding to the the touchdown, td , and liftoff, lo , events when the robot contacts and leaves the ground, respectively. The selected Poincaré section is the touchdown switching surface: \mathcal{S}_{td} , and thus the Poincaré return map is defined as $\mathcal{P} : \mathcal{S}_{td} \rightarrow \mathcal{S}_{td}$.

$$x_{td}^+[k+1] = \mathcal{P}(x_{td}^+[k]) \quad (4.11)$$

where $x_{td}^+[k+1]$ is the state following the $(k+1)$ -th touchdown event where the robot comes into contact with the ground from flight phase and $x_{td}^+[k]$ is the state. Therefore, a continual hopping motion can exist by finding a fixed point of the Poincaré return Map, which is defined by (4.12). The fixed point is numerically estimated using the `fsolve` tool in MATLAB[®].

$$x_{td}^+ = \mathcal{P}(x_{td}^+) \quad (4.12)$$

An example of the simulation results is the knee angle shown in Fig. 4.10. The figure shows the knee angle versus time throughout the hopping motion in simulation. Notice the periodicity of the knee angle which illustrates the model and computed fixed point.

An important purpose of this simulation is to find control gains that will ensure the leg reaches desired touchdown angles θ_{hip}^{des} and θ_{knee}^{des} . With the simulation results as a guideline tool for tuning the controller, simple PD control analysis for the flight phase control can ensure that the joints reach the desired touchdown angles before the touchdown event occurs. In the case of SPEAR-II, the flight phase is approximately 0.2 seconds.

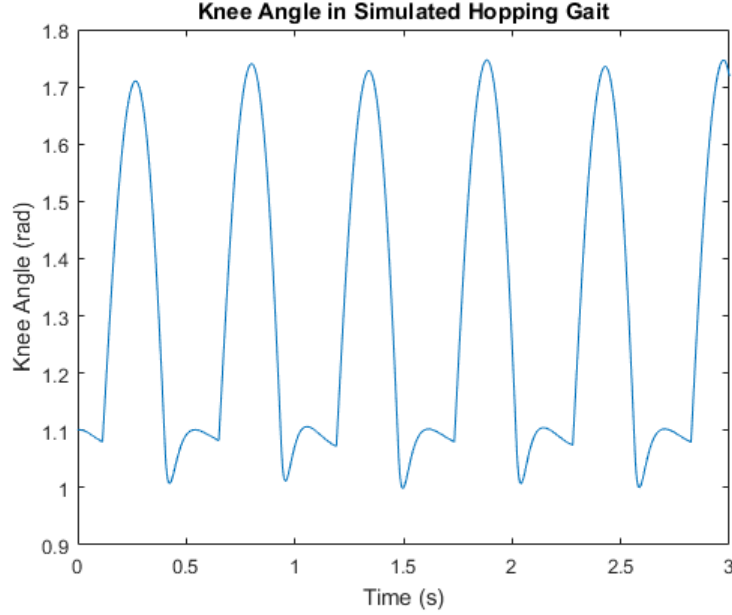


Figure 4.10: Simulation results showing the knee angle of SPEAR-II during hopping-in-place gait. Note that the PD control during flight ensures that the knee angle reaches the desired touchdown angle before touchdown.

By tuning the gains of the PD Controllers, the objective can be achieved with the following control gains: $K_{\text{hip}} = 54.77$, $K_{D_{\text{hip}}} = -1.37$ and $K_{\text{knee}} = 63.25$, $K_{D_{\text{knee}}} = -0.52$. Note that the derivative gains are negative because they are proportionate to the angular velocity of the joint, and act as an artificial damper on the knee torque. This helps the controller achieve the goal of not only reaching the desired touchdown angle, but also having ideally zero angular velocity at touchdown (such that the joint is held at the desired angle, rather than swinging into it). Lastly, the frequency f from (4.10), is calculated to be 2.56Hz.

4.3 Hopping Experiments with SPEAR-II

The work in the previous section on simulated hopping motions of the SPEAR-II model provides valuable insights for tuning controller parameters for experimentally implementing hopping. By having a more refined understanding of the interactions occurring between the elements of the Sw-PEA actuator at the knee joint, we can

improve the implementation of a control approach for hopping. The controller with the prescribed parameters discussed in the previous section are implemented on the SPEAR-II testbed to illustrate hopping-in-place.

Experimental data of SPEAR-II hopping is shown in Fig. 4.11. Both plots show the measured joint angles in blue, and the desired touchdown angles in red. The plot on the left shows the hip angle versus time, and the plot on the right shows the knee angle versus time. The plot on the right also shows a magenta dashed line which an overlay of the knee angle versus time for the simulation output shown in Fig. 4.10. The periodicity of the joint angles resemble the results of the simulation shown in Fig. 4.10. Notice the flight controllers use PD control to drive the joint angles to the desired touchdown angle, and hold the angles in place prior to touchdown.

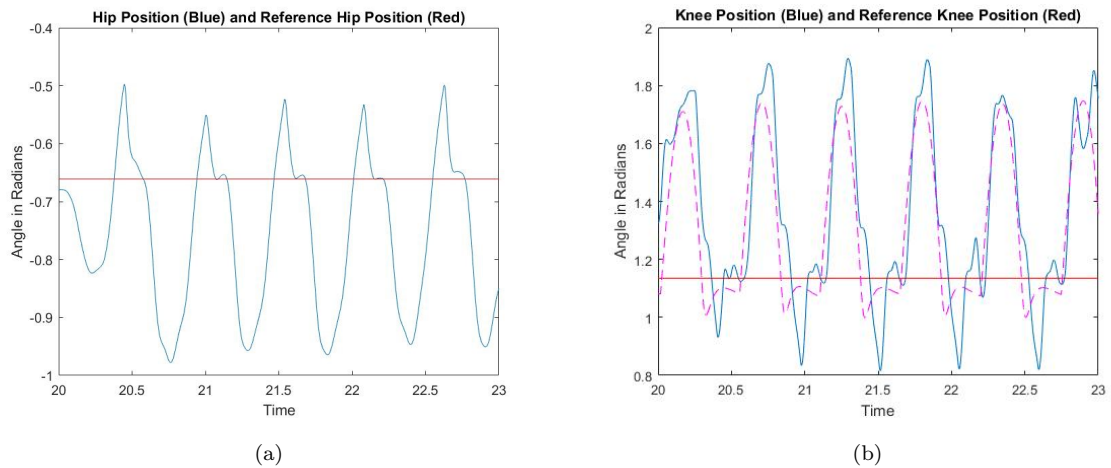


Figure 4.11: Joint angles of the Knee and Hip during hopping experiments: (a) Hip joint angle and (b) Knee joint angle

As Fig. 4.11, the output of the simulation of the controller and the model matches well with the results in the hopping experiment. Notice that despite the slight variations in trajectory, the knee angle position shown in Fig. 4.11 follows the desired behavior of the simulation output shown in Fig. 4.10.

Another measurement of interest in the hopping experiments is the current for

the motors. Fig. 4.12 shows the measured current flowing through the motors in blue, and the referenced current from the controller in red. The plot on the left is the knee current versus time, and the plot on the right is the hip current versus time. Observing the measured current in conjunction with the reference current commanded by the controller helps identify and potential issues with execution of the controller. In some instances, bugs within the electronics or issues with occasion signal loss can fault the motor drivers and yield an absence of control effort, despite the controller requesting actuation.

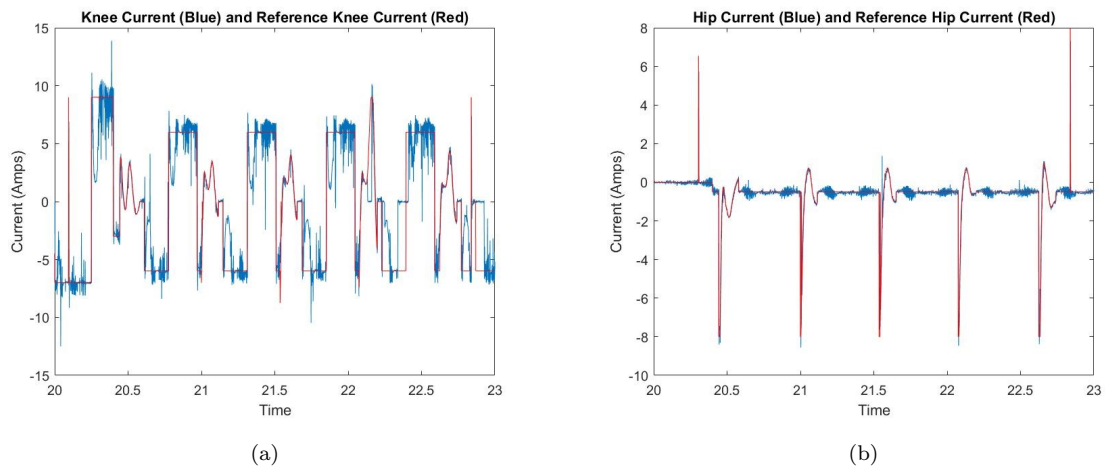


Figure 4.12: Measure and Reference Currents during hopping experiments. (a) Shows the knee current for both referenced (in red), and measured (in blue). (b) Shows the same plot for the hip current values for both referenced and measured.

While the simulated environment matches relatively closely the experiments of hopping, there is always a gap in relating a controller tuned in simulation to a live robot. Additional physical phenomena that are not modeled, such as electrical noise, and mechanical damping and vibration from the boom slider assembly, can result in deviations between experimental and simulation implementations.

Lastly, the hopping height of the hip axis is shown in Fig. 4.13. This measurement best reflects the periodic orbit of the hopping motion through the sinusoidal

plot. The noticeable variation in apex height can be attributed to the frictional damping forces and physical phenomena occurring at the boom but is not captured by the model. The controller is able to compensate and stabilize the hopping gait by injecting energy during stance. Recall in (4.10) that the knee motor helps to compress the spring during the first half of stance, and works with the spring during the second half of stance to help push off the ground. This is noticed by the higher apex height values following a decreased peak height during the previous flight phase.

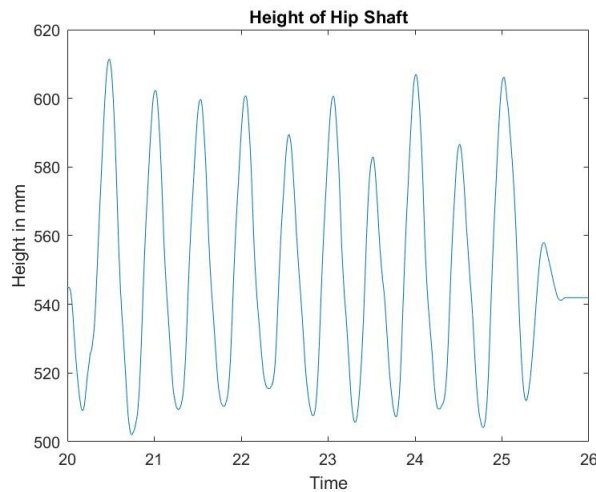


Figure 4.13: Height of the boom during an 11-hop duration experiment. Note that despite the variations of the apex height of the boom, the controller is able to respond robustly and continue the hopping gait.

Other safety features built-in to the experimental setup, while critical to preventing serious damage to the robot, can potentially have an impact on the actual performance of an experiment, relative to simulation. One nonlinearity that is implemented on live tests, but not in simulation, is saturation of the commanded current. In addition to restricting the maximum amount of current requested by the controller output, the PWM amplifiers have sophisticated on-board algorithms to prevent overheating of the motor. This can cause an unexpected loss of current during operation and can impact the performance of the robot. Despite these drawbacks, however, the

controller of Sec. 4.2.1 is shown to be robust throughout various hopping experiments, and is able to handle these disturbances to both the system and control inputs.

Chapter 5

MODELING SPEAR-II AS A LEGGED TEMPLATE IN A QUADRUPEDAL SETTING

A overarching goal is to eventually create a quadruped robot using the Sw-PEA mechanism in the legs. Implementing this actuator concept in a quadruped could create a useful combination energy efficiency with mobility and joint dexterity, for practical legged robot applications. A conceptual quadruped is proposed and shown in Fig. 5.1.

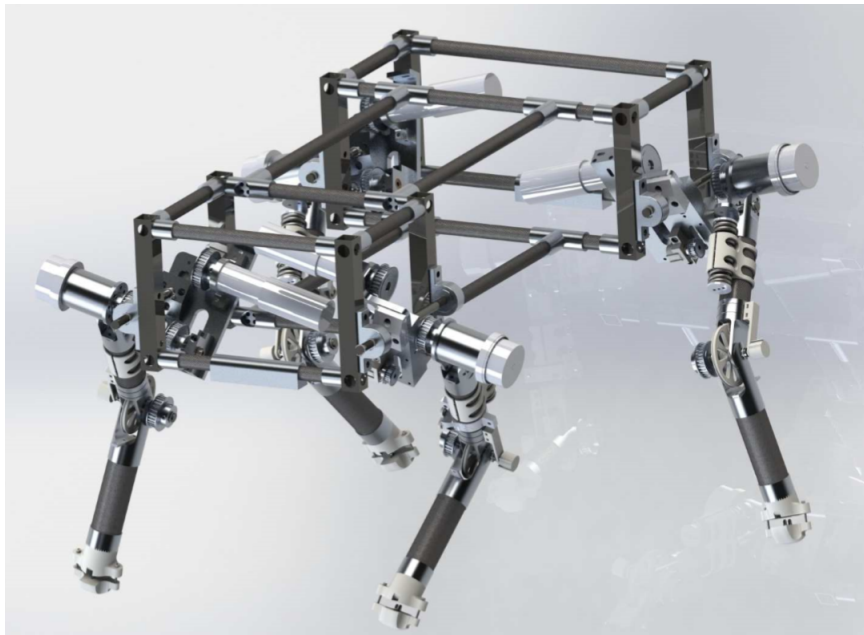


Figure 5.1: Photorealistic rendering of a 3D CAD model of a proposed quadruped using the SPEAR-II leg design.

Consider the proposed quadruped design concept in Fig. 5.1. The design uses four SPEAR-II legs in conjunction with a torso that connects them, and an added mechanism for controlling hip adduction/abduction to enable banking turns and stabilizing out of the sagittal plane. The mass properties are calculated to be $30kg$ with

electronics included, and an added $5kg$ is allowed in the model to give flexibility in future design changes. Accomplishing a design feat such as this first requires thorough analysis through simulation and development. As a starting point for this goal, this chapter will explore a preliminary analysis on the feasibility of SPEAR-II in a quadruped application.

Currently, to the author’s best knowledge, the Sw-PEA actuator has not been studied or simulated in quadrupedal running like the model proposed here. However, there are numerous existing simulation modeling and control frameworks to study and simulate quadrupedal robots with two-link legs. One of the existing frameworks provide a simulation testbed for a two-link, fully-actuated quadruped model [41]. Additionally, work has already been done to find robust controllers for these models [25]. This chapter first looks at the model of the quadruped, then applies existing methodology’s and controllers to analyze the concept of using the SPEAR-II design in a quadruped. The chapter concludes with insights from the model simulation environment, to be used as a starting point in the design process of a quadruped version SPEAR-II.

5.1 Model Overview

The motion of interest is the bounding gait. Fig. 5.2 is a diagram depicting the foot print of the quadruped during the gait. The four circles represent each of the feet on the robot. The solid black circles represent the legs in contact with the ground during stance. The white circles with black outlines represent the legs that are in the air, and are not in contact with the ground. The bounding gait consists of a posterior and anterior stance phase, with flight phases in between them. The cycle repeats itself in a periodic manner.

The model begins with the assumption that the behavior of interest can be studied by approximating the bounding motion to just the sagittal plane. This helps in reducing the order of the model well allowing for insight and understanding on the design variables of interest. The knee joints and hip joints have actuation abilities to control flexion and extension.

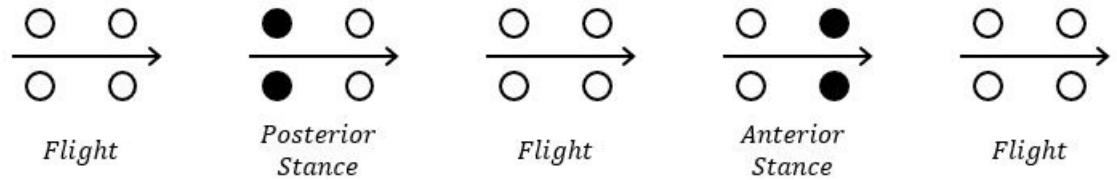


Figure 5.2: Diagram displaying the footprint during the bounding gait cycle for a quadruped.

Fig. 5.3 shows the model of the quadruped using the SPEAR-II leg design. Recall that each leg represents a pair of front and back legs and are simplified to a collective front and back leg from the sagittal plane approximation. Notice the posterior leg is shown to be in contact with the ground for stance, while the anterior leg is shown to be in the air, to illustrate the different dynamics depending on phase.

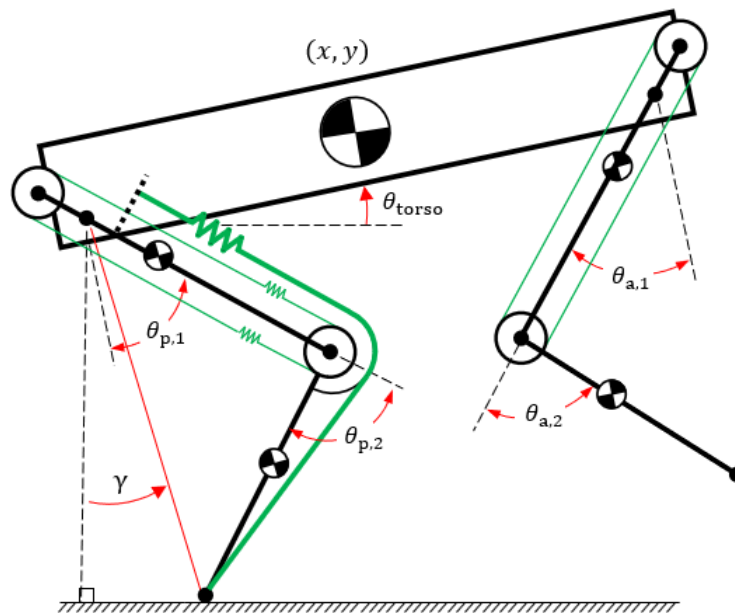


Figure 5.3: Model diagram of a quadrupedal robot using the SPEAR-II model (Q-SPEAR) as a legged platform.

Additionally, since the legs are SPEAR-II templates, there are passive compliance elements at the knee joints as part of the Sw-PEA mechanism. The subscript p denotes the posterior limb, and the subscript a denotes anterior limb. The subscripts 1 and 2 refer to the hip joint and knee joint, respectively.

Fig. 5.4 shows the transition of the 4 continuous-time phases, and 4 discrete switching events. The stance phases are the continuous-time dynamics consisting of both flights, posterior stance, and anterior stance. Between these phases, the discrete events such as liftoff and touchdown are represented by the boxes with the blue text. As described in 5.3, when a leg is in contact with the ground, the compliant elements are present in the model (and absent when a leg is no longer in contact with the ground).

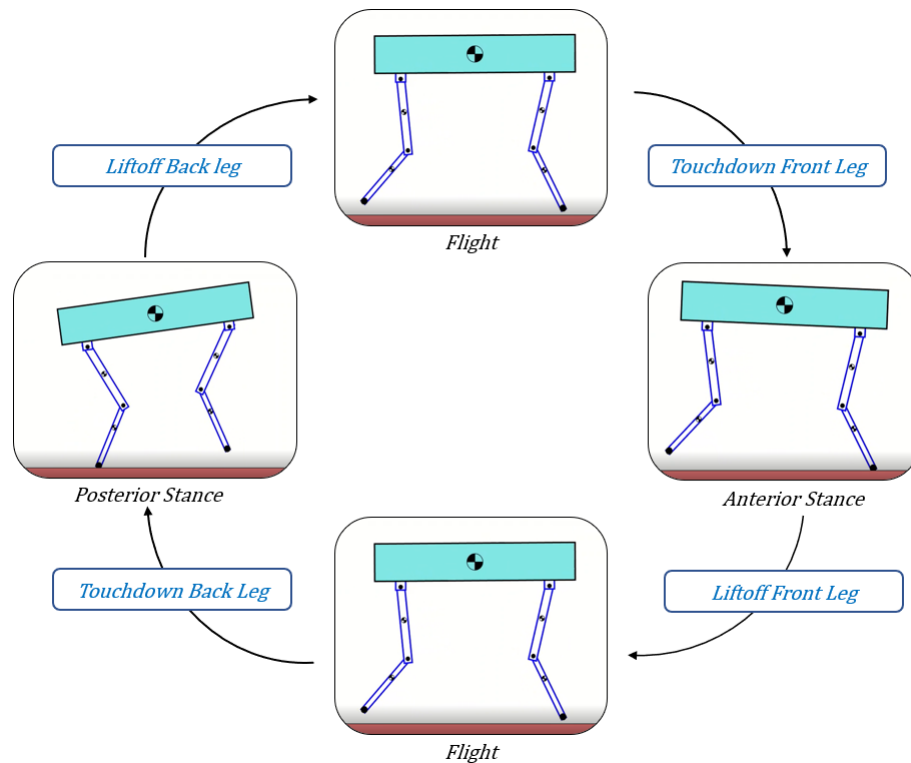


Figure 5.4: Conceptual figure of the bounding cycle for a quadrupedal robot.

The bounding gait of quadruped in this model involves four phases: two stance phases and two flight phases. The events transitioning between these phases are lift off

and touchdown events. Using the configuration variables selected in Fig.5.3, namely, $q := \{x_{\text{cm}}, y_{\text{cm}}, \theta_{\text{tor}}, \theta_{\text{p},1}, \theta_{\text{p},2}, \theta_{\text{a},1}, \theta_{\text{a},2}\}$, the dynamics of this system can be derived with the method of Lagrange in a similar fashion as in the monopedal SPEAR-II case shown of Section 3.3. The dynamics during flight can be written in the form:

$$D(q)\ddot{q} + C(\dot{q}, q)\dot{q} + G(q) = Bu + J^T F_{\text{ext}}, \quad (5.1)$$

with G being the gravitational vector, C being the Coriolis matrix, and D being the mass matrix of the system. The J^T term is used to model the impact of the leg after touchdown as an external force. Constraints are placed, regarding this term, based on a Coulomb friction model to ensure contact between the toe and the ground during stance phase. During both the posterior and anterior stance phases, the dynamics follow a similar model but with reduced order of the configuration variables. While in stance where a leg is in contact with the ground, the position of torso's center of mass can be found using the joint angles of the leg, and pitch angle of the torso.

$$D_i(q_s)\ddot{q}_s + C_i(\dot{q}_s, q_s)\dot{q}_s + G_i(q_s) = B_i u, \quad (5.2)$$

where $i \in \{\text{sp}, \text{sa}\}$ for stance posterior and stance anterior, respectively, and the configuration variables $q_s := \{\theta_{\text{tor}}, \theta_{\text{p},1}, \theta_{\text{p},2}, \theta_{\text{a},1}, \theta_{\text{a},2}\}$. Note that, similar to the monopedal case of SPEAR-II, input u not only represents the active control from the actuators, but also the passive spring torque during stance phase. Additionally, another subtlety to note exists in the D matrix due to the model accommodating the knee motor gear ratio and rotor inertia, to reflect the results of those design decisions.

Design inputs of interest are shown in Table 5.1. This includes mass properties of the torso, spring stiffness for the passive compliance component at the knee joint, and the motor and gearbox selection. With the modeling framework, and simulation environment previously discussed, multiple simulations can be performed to study the different design related inputs and the resulting performance of the quadruped.

Table 5.1: Tabulation of relevant parameters for the quadruped using SPEAR-II legs.

| Parameter | Value | Units |
|---|--------------|-------------------------|
| Torso Mass | 35 | <i>kg</i> |
| Upper Leg Mass | 1.72 | <i>kg</i> |
| Lower Leg Mass | 0.47 | <i>kg</i> |
| Total Mass | 43.76 | <i>kg</i> |
| Torso Inertia | 2.1 | <i>kg/m²</i> |
| Upper Leg Inertia (link only) | 0.014 | <i>kg/m²</i> |
| Lower Leg Inertia (link only) | 0.005 | <i>kg/m²</i> |
| Upper Leg Effective Rotor Inertia | 0.047 | <i>kg/m²</i> |
| Lower Leg Effective Rotor Inertia | 0.027 | <i>kg/m²</i> |
| $N_{kneemotor}$ | 15 | <i>unitless</i> |
| $N_{hipmotor}$ | 60 | <i>unitless</i> |
| Upper Leg Length | 0.318 | <i>m</i> |
| Lower Leg Length | 0.318 | <i>m</i> |
| Upper Leg COM to Hip Axis | 0.008 | <i>m</i> |
| Lower Leg COM to Knee Axis | 0.144 | <i>m</i> |
| Rotational Spring Stiffness (at Knee Joint) | 56 | <i>Nm/rad</i> |
| Nominal Bounding Speed (\dot{x}_{cm}) | 2.5 | <i>m/s</i> |

5.2 Controller

The controller used for bounding in the quadrupedal model is identical to the established approach shown in [25], and is used to standardize comparisons directly on the design decisions of the robot. This control scheme has been shown to be relatively robust in simulation of a similar quadruped model, and is flexible in implementation for the SPEAR-II quadruped model. To summarize, a discrete update is applied at each event to the continuous time controller. During stance phase, the control inputs for the supporting leg’s hip is held at a constant, while the control input for the knee follows a desired torque profile. While the leg is in the air, position control is implemented to ensure that the leg reaches the desired touchdown angle prior to the event.

5.2.1 Stance Control

The dynamics of the stance phase can be written, without interaction force, as

$$\dot{x}_s = f_i(x_s) + g_i^{\text{su}}(x_s)u_i^{\text{su}} + g_i^{\text{sw}}(x_s)u_i^{\text{sw}} \quad (5.3)$$

where $i \in \{sa, sp\}$ and $\dot{x}_s := (q_s', \dot{q}_s)'$ is the state vector. The functions g_i^{sw} and g_i^{su} express the influence of the support and swing leg torques u_i^{su} and u_i^{sw} on the system, respectively. In more detail, $u_{\text{sp}}^{\text{su}} = (u_{\text{p},1}, u_{\text{p},2})'$ and $u_{\text{sp}}^{\text{sw}} = (u_{\text{a},1}, u_{\text{a},2})'$ for posterior stance, and $u_{\text{sa}}^{\text{su}} = (u_{\text{a},1}, u_{\text{a},2})'$ and $u_{\text{sa}}^{\text{sw}} = (u_{\text{p},1}, u_{\text{p},2})'$ for the anterior stance.

The objective of the controller for the stance leg is to maintain contact with the ground (to enforce no slip), and to create a virtual spring force with the knee actuator to mimic the behavior of a compliant element at the joint. Mathematically, the stance controller for hip motors in the support leg follow:

$$u_{\text{p},1} = \beta_{\text{sp}} \quad \text{and} \quad u_{\text{a},1} = \beta_{\text{sa}} \quad (5.4)$$

Additionally, the stance controller for the knee motors in the support leg follows:

$$u_{\text{p},2} = \bar{u}_{\text{p},2} + k_{\text{p}}(\theta_{\text{p},2} - \bar{\theta}_{\text{p},2}) \quad (5.5)$$

for the posterior stance phase, and in a similar manner

$$u_{\text{a},2} = \bar{u}_{\text{a},2} + k_{\text{a}}(\theta_{\text{a},2} - \bar{\theta}_{\text{a},2}) \quad (5.6)$$

for the anterior stance phase. Where β_{sp} , β_{sa} , $\bar{u}_{\text{a},2}$, and $\bar{u}_{\text{p},2}$ are all constants. k_{p} and k_{a} are virtual spring stiffness values to emulate the behavior of a spring at the knee joints during stance. Lastly, $\bar{\theta}_{\text{p},2}$ and $\bar{\theta}_{\text{a},2}$ are the touchdown angles of the knee joints, and are specified as $\bar{\theta}_{\text{p},2} = -\bar{\theta}_{\text{a},2} = 40^\circ$ for consistency in liftoff.

What is important to note for the knee motor control is that the virtual spring term of the required torque can be fully or partially replaced by a physical spring at the knee joint, which is the case for SPEAR-II.

For each $i \in \text{sp,sa}$, the torque profiles for the support leg during the stance phase can be written in the form

$$u_i^{\text{su}} = \Gamma_i^{\text{su}}(x_i, \alpha_i^{\text{su}}) \quad (5.7)$$

where $i \in \{\text{sp, sa}\}$ and, $\alpha_{\text{sp}}^{\text{su}} := \{\bar{u}_{\text{p},2}, k_{\text{p}}, \beta_{\text{sp}}\}$ and $\alpha_{\text{sa}}^{\text{su}} := \{\bar{u}_{\text{a},2}, k_{\text{a}}, \beta_{\text{sa}}\}$. Using this notation, the stance dynamics shown in (5.3) for $i \in \{\text{sp, sa}\}$ with the controller of the corresponding support leg, 5.7 becomes rewritten as

$$\dot{x}_i = f_i^{\text{sw}}(x_i, \alpha_i^{\text{su}}) + g_i^{\text{sw}}(x_i)u_i^{\text{sw}} \quad (5.8)$$

where $f_i^{\text{sw}}(x_i, \alpha_i^{\text{su}}) := f_i(x_i) + g_i^{\text{su}}(x_i)\Gamma_i^{\text{su}}(x_i, \alpha_i^{\text{su}})$.

5.2.2 Swing Leg Control

During stance phase, the continuous-time control input u^{sw} in (5.8) accounts for the hip and knee joint torques of the swing leg. The purpose of this term is to ensure the swing leg is in the desired configuration and is prepared for touchdown. This is accomplished by driving the system in a prescribed manner, by associating (5.8) with the following output

$$y_i = H_i q_s - h_i^d(s_i(q_s), \alpha_i^{\text{sw}}) \quad (5.9)$$

for $i \in \text{sp,sa}$, where the vector of controlled variables $H_f q$, and the desired evolution of the controlled variables $h_i^d(s_i(q_s), \alpha_i^{\text{sw}})$, is represented by smooth polynomials which further details are shown in [25]. What is important is that the polynomials are parameterized by normalized variables

$$s_{\text{sp}}(q_{\text{sp}}) := \frac{\gamma_{\text{p}}(q_{\text{sp}}) - \gamma_{\text{p}}^{\text{td}}}{\Delta_{\text{sp}}} \quad \text{and} \quad s_{\text{sa}}(q_{\text{sa}}) := \frac{\gamma_{\text{a}}(q_{\text{sa}}) - \gamma_{\text{a}}^{\text{td}}}{\Delta_{\text{sa}}} \quad (5.10)$$

where Δ_{sp} and Δ_{sa} are constants, $\gamma_{\text{p}}^{\text{td}}$ and $\gamma_{\text{a}}^{\text{td}}$ are the angles between the line directly connecting the hip joint to the foot (of the posterior or anterior leg, respectively) and the vertical; see Fig. 5.3. $\gamma_{\text{p}}^{\text{td}}$ and $\gamma_{\text{a}}^{\text{td}}$ are the corresponding values at touchdown.

The parameters associated with constructing the desired evolution h_i^d of the controlled variables, are collected in the array α_i^{sw} and plays a role in defining the constraint (5.8).

Since the outputs (5.8) are functions of only the configuration variables, they can be interpreted as holonomic constraints, and can be imposed on the system by driving the outputs (5.8) to zero. By differentiating (5.8) for given values of $\alpha_i := \{\alpha_i^{su}, \alpha_i^{sw}\}$ we get

$$\frac{d^2 y_i}{dt^2} = L_{f_i^{sw}}^2 h_i(x_i, \alpha_i) + L_{g_i^{sw}} L_{f_i^{sw}} h_i(x_i, \alpha_i) u^{sw} \quad (5.11)$$

where $L_{g_i^{sw}} L_{f_i^{sw}} h_i(x_i, \alpha_i)$ is the decoupling matrix. Upon verifying the invertibility of $L_{g_i^{sw}} L_{f_i^{sw}} h_i(x_i, \alpha_i)$,

$$u_*^{sw}(x_i, \alpha_i) := -(L_{g_i^{sw}} L_{f_i^{sw}} h_i(x_i, \alpha_i))^{-1} L_{f_i^{sw}}^2 h_i(x_i, \alpha_i) \quad (5.12)$$

is the unique control input which renders the surface

$$\mathcal{Z}_{\alpha_i} := \{x_i \in \mathcal{X}_i \mid h_i(q_i, \alpha_i^{sw}) = 0, L_{f_i^{sw}} h_i(x_i, \alpha_i) = 0\} \quad (5.13)$$

invariant under the flow of the closed-loop dynamics. Zeroing the output effectively reduces the dimension of the system by restricting its dynamics on the zero dynamics surface \mathcal{Z}_{α_i} . The dynamics of the system restricted on \mathcal{Z}_{α_i} ,

$$\dot{z} = f_i^*|_{\mathcal{Z}_{\alpha_i}}(z) \quad (5.14)$$

is the corresponding zero dynamics. In order to ensure attractivity of \mathcal{Z}_{α_i} , the input (5.12) shall be modified to be

$$u^{sw} = \Gamma_i^{sw}(x_i, \alpha_i) = (L_{g_i^{sw}} L_{f_i^{sw}} h_i(x_i, \alpha_i))^{-1} [v(y_i, \dot{y}_i, \epsilon) - L_{g_i^{sw}} L_{f_i^{sw}} h_i(x_i, \alpha_i)] \quad (5.15)$$

where

$$v(y_i, \dot{y}_i, \epsilon) := -\frac{1}{\epsilon^2} K_P y_i - \frac{1}{\epsilon} K_V \dot{y}_i \quad (5.16)$$

and K_P , K_V are gain matrices, and $\epsilon > 0$. Using continuous-time feedback laws Γ_i^{sw} for $i \in \text{sp,sa}$, the solutions of 5.8 converge to the invariant surface \mathcal{Z}_{α_i} exponentially fast.

5.2.3 Flight Phase Controller

The continuous-time controller in the flight phases are analogous to that of the control design in the stance phase. Consider the dynamics for both flight phases, to be written as

$$\dot{x}_f = f_f(x_f) + g_f(x_f)u \quad (5.17)$$

where $x_f := (q', \dot{q}')'$ is the state for the flight phase. In order to implement the use of polynomials with different coefficients in defining the desired evolution of the controlled variables, we associate the output

$$y_i = h_i(x_f, \alpha_i) := H_f q - h_i^d(s_{f(q), \alpha_i}) \quad (5.18)$$

where $i \in \{f_1, f_2\}$. The controlled variables $H_f q$ are the same in both phases of flight, and correspond with the absolute and relative knee angles of the posterior and anterior legs.

For each flight phase $i \in \{f_1, f_2\}$, h_i^d represents the desired evolution of the controlled variables, which is (similar to the swing leg controller) defined by smooth polynomials which are parameterized by the monotonic quantity

$$s_i(q_i) = \frac{x_{\text{cm}} - x_{\text{cm},i}^{\text{lo}}}{\Delta_i} \quad (5.19)$$

where Δ_i is a constant used to normalize, and $x_{\text{cm},i}^{\text{lo}}$ is the value of the horizontal coordinate x_{cm} of the torso's COM at liftoff. Similar to the swing leg control section, more details around the description of the polynomials can be found in [25].

A continuous-time controller that zeros the output (5.18) is designed to impose the constraints. The procedure is similar to that of the swing leg control during stance phase. The corresponding controller, in each phase $i \in f_1, f_2$, has the following form

$$u = \Gamma_i^c(x_f, \alpha_i) := (L_{g_f} L_{f_f} h_i(x_f, \alpha_i))^{-1} [v(y_i, \dot{y}_i, \epsilon) - L_{g_f} L_{f_f} h_i(x_f, \alpha_i)] \quad (5.20)$$

where the control input v has the same form as (5.16), and it similarly renders the zero dynamics surface

$$\mathcal{Z}_{\alpha_i} = x_f \in \mathcal{X}_f \mid h_i(q_f, \alpha_i) = 0, L_{f_f} h_i(x_f, \alpha_i) = 0 \quad (5.21)$$

invariant and attractive.

5.2.4 Discrete-time Control Laws

An important component of the controller is the update of parameters in the continuous-time controllers, at each discrete transition. At discrete transitions, zeroing of the output may be violated when $x^+ \in \mathcal{Z}_{\alpha_i}$ for $i \in \{\text{sp}, \text{sa}, f_1, f_2\}$. After transition, the state of the robot is x_i^+ . In order to ensure that the zero dynamics surface is invariant for each phase under transitions, the following control action is used to update the parameters α_i , according to the respective controller

$$\alpha_i^+ = \Gamma_i^\alpha(x_i^+) \quad (5.22)$$

for $i \in \{\text{sp}, \text{sa}, f_1, f_2\}$. Further details relating to the parameters are shown in [25].

5.3 Analysis of Results

The simulation highlights interesting results regarding the application of the SPEAR-II on a quadruped platform, as well as the robust controller for the quadruped. The highlighted findings regarding the benefit of the Sw-PEA in a quadruped are seen in Fig. 5.5. Notice that the passive compliant component of the actuator reduces the peak torque requirement of the motor, as expected. While the results show promising

potential for the SPEAR-II leg design concept to be used for a quadruped, there are still many practical considerations that are noted from the simulation results that will need to be addressed in order to move forward. The dashed red line illustrates a simulated quadruped using the mass and geometry properties of SPEAR-II but without the passive spring element at the knee. The blue line represents the current SPEAR-II model, as is, on a quadruped.

An important result of the simulation effort is to review the control effort required by the actuators. Fig. 5.5 is an example of this by showing the required torques provided by the knee motors in order to sustaining the bounding motion of the quadruped. The knee torque required for the front leg is shown in the plot on the left, and the required knee torque for the back leg is shown in the plot on the right. The red dashed line in the figure represents the total required torque at the joints for the bounding motion, regardless of whether or not a spring is present at the joint. This data set is labeled “SPEAR-II No Compliance” because it represents the required torque for the SPEAR-II leg without the passive spring. The benefit of having compliance at the knee joint is shown by the blue line, labeled “SPEAR-II Model”, where the peak torque during stance is reduced. This is due to the required torque for bounding is distributed across the motor and spring, where they essentially work in an additive fashion to provide the total torque.

An overall theme from the simulation results of the quadruped highlight the relative large change of magnitude in inertia properties from scaling up a monopod design to a quadrupedal concept, and hence consequential design decisions. The root of this issue is the effect of the torso properties and added dynamic behavior from gaits such as bounding. In the monopod version of SPEAR-II, the mass supported by the leg (not including the leg itself) is the boom which is $4.6kg$. However, for the baseline quadruped model using SPEAR-II, the torso is $35kg$ which translates to a nominal $8.75kg$ per leg in static case. Additionally, with dynamic nature of a bounding gait, the required torques at the joints will be much larger than the ones anticipated in the static case. This illustrates a need for added consideration future design work related to

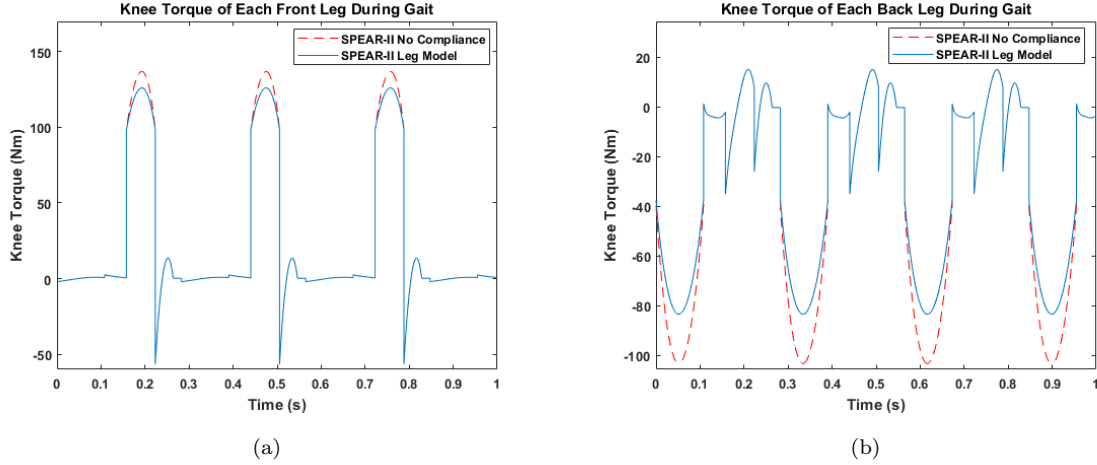


Figure 5.5: Plots showing the commanded knee torques from the motors for both the front (a) and back (b) legs throughout the simulation.

a quadruped using SPEAR-II. In fact, in various simulations using different gear ratios for the knee motor, the reflected inertia had a much smaller impact on the performance in comparison to a change in inertia of the torso.

Furthermore, the simulation framework shows the possibility of fine-tuning the mechanical design such that the actuator effort at the knee joint is minimal during the stance phase, which is the most demanding phase.

Fig. 5.6 shows the ability of the passive spring to reduce the effort of the motor while still maintaining the total required torque to sustain the bounding motion. The vertical axis represents the torque supplied by the knee motor and the horizontal axis shows the time during the simulation. The blue line shows the total torque required at the knee joint for bounding. The red line shows the prescribed knee torque for the SPEAR-II leg model. Additionally, the spring stiffness increased to illustrate the effect of having the motor effort reduced, as the spring begins to provide more a larger contribution of the total required torque at the knee joint. This is shown by the yellow, purple, and green lines in the figure, which correspond to k_{Rot} stiffness values of 200, 300, and $400 \frac{Nm}{rad}$ respectively. Notice that the yellow line is flattened due to the spring

force matching the exact amount from the virtual spring force in the controller shown in (5.6) and (5.5).

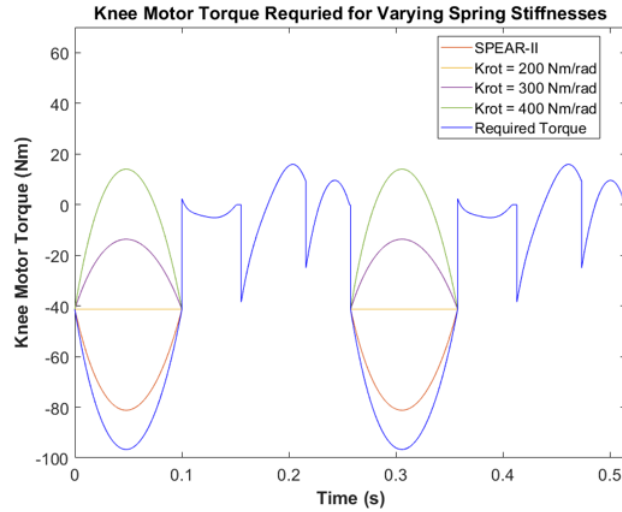


Figure 5.6: Plot showing the required knee torque for a variety of spring stiffness versus time.

5.4 Considerations for Quadruped Design

A major design improvement for a quadrupedal SPEAR robot (Q-SPEAR), would be to further reduce the peak torque requirement of the knee motor during stance phase. Fortunately, this can be implemented rather simply by replacing the current spring in SPEAR-II with one that is at least twice the linear stiffness. This will reduce the peak torques applied by the knee motor during stance phase, shown in Fig. 5.5(b) to roughly $40Nm$. A design decision like this highlights a key benefit of the Sw-PEA in this setting, where the passive compliant element can be selected specifically for tasks like bounding.

While the passive element can reduce the peak torque requirement of the knee motor, it will have little, if any, effect on the hip motor requirements since the Sw-PEA is implemented at the knee joint only. The torque requirements at the hip cannot be reduced by the spring at the knee joint. Fig. 5.7 shows the torque from the hip motors versus time. The plot on the left shows the hip motor torque for the front leg, and

the plot on the right is the hip motor torque for the back leg. Recall that the main objective of the control effort for the hip motors are to drive the leg angles to the desired touchdown configuration prior to the touchdown event.

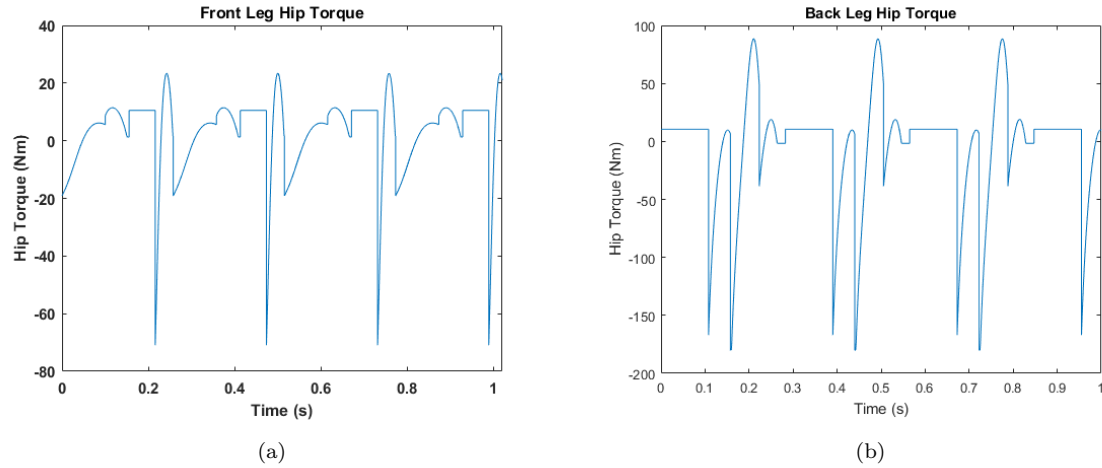


Figure 5.7: Hip motor torques specified by the controller

From the simulation results shown in Fig. 5.7, it is noted that the torque requirements are higher than what would be extrapolated from the monopodal analysis. As is, the current hip motor specifications would not be able to provide the peak torques shown in the results. Since the current motor at the hip can conceal its long cylindrical geometry in the torso, and has a relatively low rotor inertia (which reduces the backdrivability issues discussed in Chapter 4 for the knee motor), the gearbox can be doubled from the current 60:1 ratio. Also note that the hip motor's actuation effort is relatively small in comparison to the actuation effort of the knee motor. This is easy to do from a design perspective, and is available off-the-shelf from current manufacturer of the hip motor on SPEAR-II. The issues of backdrivability and reflected inertia discussed in Chapter 4 are not as much a concern for the hip motor, as it is for the knee motor in this design.

The data points from the simulation relating to the motor torques and speeds.

By reviewing the simulation results, the requirements of from the knee motors can be observed by plotting the torque and speed of the joint, and comparing with the capabilities of a prospective motor. This can provide an understanding of whether or not a potential motor can meet the demands of the quadrupedal bounding gait. An example of this is shown in Fig. 5.8, where the torques and speeds of the knee joint are plotted as a scatter plot in the blue “x” points. The current 100W Maxon motor cannot provide sufficient power to the knee joints for the quadrupedal bounding gait, therefore two prospective motors are selected as candidates for the quadrupedal design; one rated at 260W and the other at 600W. The maximum limit of the prospective motors are shown by the solid black and green lines, for the 260W and 600W motors, respectively. Note that the motor can only provide for the torque/speed pair of data points which are less than the solid lines.

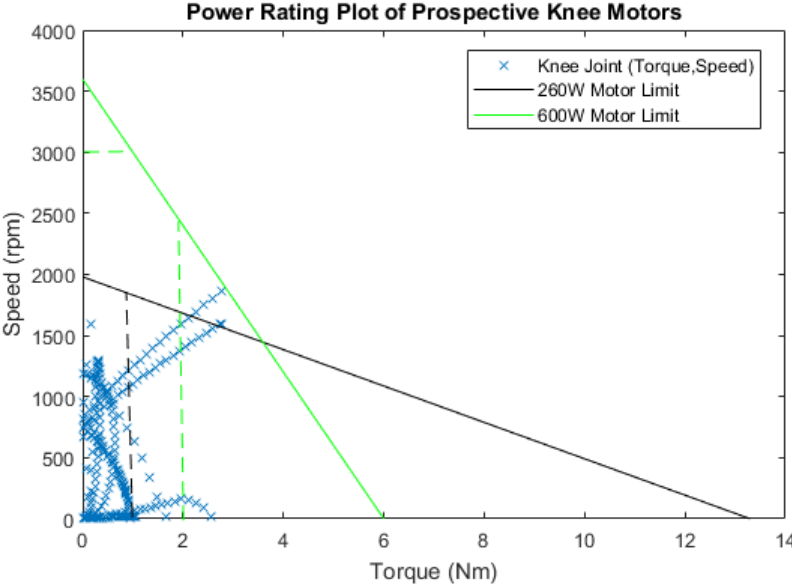


Figure 5.8: Plot of data points of the required torque/speed pairs from the knee joint and prospective motor operating ranges to assess feasibility.

Additionally, Fig. 5.8 shows dashed vertical and horizontal lines to show the boundaries of the continuous operation range. This is the area (less than the dashed

lines) of torques and speeds which the motor can continuously supply without overheating. Often, the motors can be operated outside the continuous operation range for intermittent use; which is done in both the SPEAR-I and SPEAR-II case. From the blue “x” data points shown in relation to the motor operating ranges, the proposed 260W motor cannot provide the adequate amount of power for a few of the data points; where the points exceed the solid black line. The prospective 600W motor can provide the necessary power to sustain quadrupedal bounding.

An interesting note regarding the results shown in Fig. 5.8 is that the peak torque requirements which exceed the 260W motor limit is from the brief time after the leg touches down and lifts off. This is due to the nominal knee torque applied to maintain contact of the foot with the ground to prevent slipping; that is $\bar{u}_{p,2}$ and $\bar{u}_{a,2}$ in (5.5) and (5.6), respectively. There is a possibility of design a controller which can reduce the magnitude of $\bar{u}_{p,2}$ and $\bar{u}_{a,2}$, by changing the touchdown angles of the legs. Additionally, the design of the foot could ensure a high friction coefficient between most ground surfaces and the toe, which could justify lower nominal torques in (5.5) and (5.6) while preventing slipping. These changes with regard to the controller, and foot surface design, could enable the selection of the 260W motor. This would be ideal since this motor is essentially a slightly larger version of the current SPEAR-II knee motor, with a higher power rating, but with similar mass and inertia properties. However, if the 260W motor cannot be made feasible, then an off-the-shelf 600W motor has been identified and can support the requirements of quadruped. The drawback is that this prospective motor is significantly heavier than the current design on SPEAR-II. For either case, an additional consideration for using the SPEAR-II design in the quadruped is to reinforce the strength of the foot assembly since the new torques from the upgraded motor and spring will be larger than the SPEAR-II monopod setting.

Chapter 6

CONCLUSIONS AND FUTURE WORK

6.1 Conclusions

Compromise between mobility and energy-efficiency has been better addressed in legged robots using the Sw-PEA actuator at the knee joint. While previous designs which address this have taken steps of progress, additional work towards developing a quadruped using the Sw-PEA actuator and the SPEAR template was needed as a preliminary step. This thesis contributed in this overall goal by bridging some of the gaps between a monopedal robot design to creating a functional quadruped. Overall, the SPEAR-II design effort was successful in achieving the objectives set forth in Chapter 2. As shown in the analysis of the design, there were some design drawbacks related to added friction and increased reflected knee rotor inertia. Additionally, analysis from the simulation of the quadruped highlights the need to upgrade the power rating of the motors on SPEAR-II, as well as increasing the stiffness of spring S_1 ; which consequentially requires reinforcing the foot to increase the strength for the larger forces in the quadruped.

This thesis began with a revised design of the original SPEAR robot with the objective of creating a template that can be used for a quadruped. SPEAR-II was designed to address the drawbacks of first iteration such as limited range of motion, relatively higher mass and inertia, and additional design complexity. SPEAR-II was designed with a more concise and simplified geometry, lighter-weight materials, improved transmission mechanisms, a new knee motor with a compact footprint, and a new boom design to support the leg for testing.

Next, a model describing the physical interactions of the new SPEAR-II design is constructed to represent finer details of the robot, which were previously not addressed.

This includes the higher resolution understanding of the transmission mechanism and the implications of motor and gearbox selection, as well as a deeper understanding of the electromechanical interactions. With this modeling structure, a parameter identification technique was created and implemented to fine-tune the model giving it a more accurate representation of the SPEAR-II leg. The updated model was then analyzed using simulation to tune a hopping controller for the monopod. Lastly, this controller was implemented on the experimental testbed to validate the model with hopping experiments.

Finally, the thesis proposes a quadruped model using the SPEAR-II leg template. The objective of the simulation is to evaluate the feasibility from a dynamics and control perspective, of whether the current design can be used with its existing specifications. With some very minor modifications, the use of SPEAR-II for a quadruped is shown to be likely a successful combination for a proposed design.

6.2 Future Work

6.2.1 Design of QSPEAR Quadruped

This thesis has taken the Sw-PEA concept, and SPEAR-II design closer to adaptation for a quadruped design. Constructing a quadruped using SPEAR-II as a leg design template, and successfully demonstrating a bounding gait would bring the Sw-PEA concept to a testbed which can show the benefits of the design in practical applications. While the proposed quadruped design concept, and the corresponding analysis work show in Chapter 5, illustrate the feasibility of the current hardware specifications, there are additional steps required before manufacturing the quadruped.

In addition to the required modifications found in Chapter 5, the remaining tasks are primarily centered around the mechanical design of the torso and 3rd DOF mechanism. Similar analysis to the work shown in Chapter 4 will be needed to develop a model of the actuation of the hip adduction/abduction motion. Fortunately, for banking turns and other desirable motions using the 3rd DOF, the speed requirements and required range of motion for the actuator are relatively low compared to a more

complicated joint like the knee. Additionally, packaging the on-board electronics in a compact, yet safe (from damage due to impacts, etc.), manner will be necessary prior to finalizing design plans.

6.2.2 Regenerative Braking and Backdriving Experiments

The understanding of the effects of reflected inertia due to motor and gearbox selection were discussed in Chapter 4, and illustrated the mechanical effects of the design decisions. Additionally, Chapter 4 shows a model of the electromechanical interactions which considers scenarios that would cause electrical power generation due to the passive spring element transmitting mechanical power through the knee joint. It is known, and shown, that when zero current is commanded, the switches in the H Bridge circuitry on the motor drivers are open, thus making the motor a no-load generator. Additionally, when current is commanded, and the motor is forced in an opposite direction to the flow of the current, there is a possibility of regenerative braking. This would present the opportunity to combine the mechanical energy-storing capabilities of Sw-PEA, with electrical energy-efficiency approaches such as the regenerative braking concepts shown in [42],[43],[44].

While it is understood that this can occur in certain scenarios, it would be an interesting next step to quantify the effect for use in future energy-related calculations of a robot or controller design. The nominal voltage calculation using the motor constants in Chapter 4 are considered an ideal approximation due to the fact that the PWM amplifiers have their own PID control loops internally to regulate the flow of current to the motors. Additional experiments, similar to the Parameter Identification Experiments shown in Chapter 4, could be conducted to isolate this effect and measure the corresponding power flow. Also, added measurement devices would need to probe various parts of the PWM amplifiers to obtain real-time measurements of the voltage and current during these experiments.

6.2.3 Effects of Monopod Boom

SPEAR-II featured a testbed setup that differed fundamentally from its predecessor SPEAR. The boom design in the current application had benefits of simplified, accurate measurement of height and planar velocities due to the Cartesian-based geometry of the design. Previously, the boom was a rotational concept that derives its measurements from Spherical-based coordinates with a fixed radius of the boom's arm length. While the re-design helped address the measurement problem, it created an issue of added friction due to increased contact area with the moving parts. This is noticed in Chapter 4 in the Parameter Identification work, where the damping coefficient for the lumped boom and system without the knee actuator is found to be 4x larger than the damping coefficient of the knee actuator and transmission mechanism. Changing out the robots to run experiments with different booms, while difficult due to the lack of modular design in the first iteration, would be interesting to assess and understand for future legged robot designs. In order to compare the effect of the different boom designs, the SPEAR-I boom would need significant modifications to make the equipment modular. Modularity in the boom design would enable a simple means of connecting and disconnecting both SPEAR-I and SPEAR-II with regard to the electronics, as well as the mechanical mounting. Analyzing the effects of the boom can help a designer account for added interactions that are external to the leg design itself, and can help in developing templates for quadruped, and even biped, applications.

6.2.4 Biped using SPEAR-II

An interesting implementation of the SPEAR-II design would be in a Biped setting. In addition to the energetic efficient aspect, the potential of tuning the effective stiffness by changing the configuration of the leg at touchdown (see [26, 25, 27]) presents interesting research. Ideally, the biped could be built by creating two SPEAR-II legs, and designing a torso which houses the electronics and connects the two legs. With lower total mass and less impulsive dynamics, in comparison to a quadruped and a corresponding bounding gait, it is likely that the motors on SPEAR-II would not

have to be upgraded for the proposed biped concept. This would make for a quicker implementation to test the concept as a hardware realization.

BIBLIOGRAPHY

- [1] R. McN. Alexander. Three Uses for Springs in Legged Locomotion. *Int. J. Robot. Res.*, 9(2):53–61, 1990.
- [2] A. Ananthanarayanan, M. Azadi, and S. Kim. Towards a bio-inspired leg design for high-speed running. *Bioinspiration & Biomimetics*, 7(4):1–12, 2012.
- [3] W. R. Brown and A. G. Ulsoy. A maneuver based design of a passive-assist device for augmenting active joints. *J. of Mechanisms and Robotics*, 5(3):031003 1–11, 2013.
- [4] Q. Cao and I. Poulakakis. Passive quadrupedal bounding with a segmented flexible torso. In *Proceedings of the IEEE/RSJ International Conference on Intelligent Robots and Systems*, pages 2484–2489, 2012.
- [5] Q. Cao and I. Poulakakis. Quadrupedal bounding with a segmented flexible torso: passive stability and feedback control. *Bioinspiration & Biomimetics*, 8(4):046007, 2013.
- [6] S. Diller, C. Majidi, and S. H. Collins. A lightweight, low-power electroadhesive clutch and spring for exoskeleton actuation. In *Proc. IEEE Int. Conf. Robot. Autom.*, pages 682–689, 2016.
- [7] G. Elliott, A. Marecki, and H. Herr. Design of a clutch–spring knee exoskeleton for running. *J. Med. Devices*, 8(3):031002, 2014.
- [8] M. Eslamy, M. Grimmer, and A. Seyfarth. Effects of unidirectional parallel springs on required peak power and energy in powered prosthetic ankles: Comparison between different active actuation concepts. In *Proc. IEEE Int. Conf. Robot. Biomimetics*, pages 2406–2412, 2012.
- [9] G. A. Folkertsma, S. Kim, and S. Stramigioli. Parallel stiffness in a bounding quadruped with flexible spine. In *Proc. IEEE/RSJ Int. Conf. Intell. Robots Syst.*, pages 2210–2215, 2012.
- [10] R. Furnémont, G. Mathijssen, T. Verstraten, D. Lefeber, and B. Vanderborght. Bi-directional series-parallel elastic actuator and overlap of the actuation layers. *Bioinspiration & biomimetics*, 11(1):1–18, 2016.

- [11] M. Grimmer, M. Eslamy, S. Gliech, and Booktitle = Proc. IEEE Int. Conf. Robot. Autom. Year = 2012 Pages = 2463-2470 Seyfarth, A. A comparison of parallel-and series elastic elements in an actuator for mimicking human ankle joint in walking and running.
- [12] K. Harada, E. Yoshida, and K. Yokoi, editors. *Motion Planning for Humanoid Robots*. Springer-Verlag, 2010.
- [13] D. F.B. Häuffe, M.D. Taylor, S. Schmitt, and H. Geyer. A clutched parallel elastic actuator concept: towards energy efficient powered legs in prosthetics and robotics. In *IEEE Int. Conf. on Biomedical Robotics and Biomechatronics*, pages 1614–1619, 2012.
- [14] M. A. Holgate, J. K. Hitt, R. D. Bellman, T. G. Sugar, and K. W. Hollander. The SPARKy (spring ankle with regenerative kinetics) project: Choosing a dc motor based actuation method. In *IEEE Int. Conf. on Biomedical Robotics and Biomechatronics*, pages 163–168, 2008.
- [15] C. Hubicki, J. Grimes, M. Jones, D. Renjewski, A. Sprowitz, A. Abate, and J. Hurst. Atrias: Design and validation of a tether-free 3d-capable spring-mass bipedal robot. *Int. J. Robot. Res.*, 35(12):1497–1521, 2016.
- [16] J. W. Hurst. *The Role and Implementation of Compliance in Legged Locomotion*. PhD thesis, Carnegie Mellon University, 2008.
- [17] J. W. Hurst and A. Rizzi. Series compliance for an efficient running gait. *IEEE Robot. Autom. Mag.*, 15(3):42–51, 2008.
- [18] M. Hutter. *StarlETH & Co-Design and Control of Legged Robots with Compliant Actuation*. PhD thesis, ETH Zurich, 2013.
- [19] M. Hutter, C. Gehring, M. A. Höpfinger, M. Blösch, and R. Siegwart. Toward combining speed, efficiency, versatility, and robustness in an autonomous quadruped. *IEEE Trans. Robot.*, 30(6):1427–1440, 2014.
- [20] M. Hutter, C. D. Remy, M. A. Hoepfänger, and R. Siegwart. Efficient and versatile locomotion with highly compliant legs. *IEEE/ASME Trans. Mechatronics*, 18(2):449–458, 2013.
- [21] J. G. D. Karssen. *Robotic Bipedal Running: Increasing disturbance rejection*. PhD thesis, Delft University of Technology, 2013.
- [22] A. D. Kuo. Choosing your steps carefully: Trade-offs between economy and versatility in dynamic walking bipedal robots. *IEEE Robot. Autom. Mag.*, 14(2):18–29, 2007.

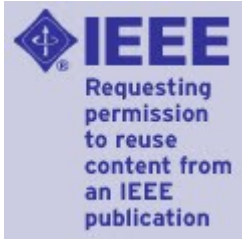
- [23] D. Leach, F. Gunther, N. Maheshwari, and F. Iida. Linear multimodal actuation through discrete coupling. *IEEE/ASME Trans. Mechatronics*, 19(3):827–839, 2014.
- [24] Z. Li, N. G. Tsagarakis, and D. G. Caldwell. A passivity based admittance control for stabilizing the compliant humanoid COMAN. In *IEEE Int. Conf. on Humanoid Robots*, pages 43–49, 2012.
- [25] X. Liu. *Harnessing Compliance in the Design and Control of Running Robots*. PhD thesis, University of Delaware, 2017.
- [26] X. Liu, A. Rossi, and I. Poulakakis. SPEAR: A monopedal robot with switchable parallel elastic actuator. In *Proc. IEEE/RSJ Int. Conf. Intell. Robots Syst.*, pages 5142–5147, 2015.
- [27] X. Liu, A. Rossi, and I. Poulakakis. A switchable parallel elastic actuator and its application to leg design for running robots. *IEEE/ASME Trans. Mechatronics*, 23(6):2681–2692, 2018.
- [28] G. Mathijssen, D. Lefeber, and B. Vanderborght. Variable recruitment of parallel elastic elements: Series–parallel elastic actuators (spea) with dephased mutilated gears. *IEEE/ASME Trans. Mechatronics*, 20(2):594–602, 2015.
- [29] U. Mettin, P. X. La Hera, L. B. Freidovich, and A. S. Shiriaev. Parallel elastic actuators as control tool for preplanned trajectories of underactuated mechanical systems. *Int. J. Robot. Res.*, 29(9):1186–1198, 2009.
- [30] N. Paine, S. Oh, and L. Sentis. Design and control considerations for high-performance series elastic actuators. *IEEE/ASME Trans. Mechatronics*, 19(3):1080–1091, 2014.
- [31] M. Plooiij, G. Mathijssen, P. Cherelle, D. Lefeber, and B. Vanderborght. Lock your robot: A review of locking devices in robotics. *IEEE Robot. Autom. Mag.*, 22(1):106–117, 2015.
- [32] M. Plooiij, M. van Nunspeet, M. Wisse, and H. Vallery. Design and evaluation of the bi-directional clutched parallel elastic actuator (bic-pea). In *Proc. IEEE Int. Conf. Robot. Autom.*, pages 1002–1009, 2015.
- [33] C. M. Pollock and R. E. Shadwick. Relationship between body mass and biomechanical properties of limb tendons in adult mammals. *Am. J. of Physiology-Regulatory, Integrative and Comparative Physiology*, 266(3):R1016–R1021, 1994.
- [34] Ioannis Poulakakis, James Andrew Smith, and Martin Buehler. Modeling and experiments of untethered quadrupedal running with a bounding gait: The scout ii robot. *Int. J. Robot. Res.*, 24(4):239–256, 2005.

- [35] G. A. Pratt and M. M. Williamson. Series elastic actuators. In *Proc. IEEE/RSJ Int. Conf. Intell. Robots Syst.*, pages 399–406, 1995.
- [36] M. H. Raibert. *Legged Robots that Balance*. MIT Press, 1986.
- [37] M. H. Raibert, K. Blankespoor, G. Nelson, R. Playter, and the BigDog Team. BigDog, the rough-terrain quadruped robot. In *Proc. of the 17th IFAC World Congress*, pages 10822–10825, 2008.
- [38] E. J. Rouse, L. M. Mooney, and H. M. Herr. Clutchable series-elastic actuator: Implications for prosthetic knee design. *Int. J. Robot. Res.*, 33(13):1611–1625, 2014.
- [39] P. Scholl, V. Grabosch, M. Eslamy, and A. Seyfarth. Comparison of peak power and energy requirements in different actuation concepts for active knee prosthesis. In *IEEE Int. Conf. on Mechatronics and Automation*, pages 1448–1453, 2015.
- [40] C. Semini, V. Barasuol, T. Boaventura, M. Frigerio, M. Focchi, D. G. Caldwell, and J. Buchli. Towards versatile legged robots through active impedance control. *Int. J. Robot. Res.*, 34(7):1003–1020, 2015.
- [41] C. Semini, N. G. Tsagarakis, E. Guglielmino, M. Focchi, F. Cannella, and D. G. Caldwell. Design of HyQ - a hydraulically and electrically actuated quadruped robot. *Proceedings of the IMechE Part I: Journal Systems and Control Engineering*, 225(6):831–849, 2011.
- [42] S. Seok, A. Wang, M. Y. Chuah, D. J. Hyun, J. Lee, D. Otten, J. Lang, and S. Kim. Design principles for energy-efficient legged locomotion and implementation on the MIT cheetah robot. *IEEE/ASME Trans. Mechatronics*, 20(3):1117–1129, 2015.
- [43] S. Seok, A. Wang, M. Y. Chuah, D. Otten, J. Lang, and S. Kim. Design principles for highly efficient quadrupeds and implementation on the mit cheetah robot. In *Proc. IEEE Int. Conf. Robot. Autom.*, pages 3307–3312. IEEE, 2013.
- [44] S. Seok, A. Wang, D. Otten, and S. Kim. Actuator design for high force proprioceptive control in fast legged locomotion. In *Proc. IEEE/RSJ Int. Conf. Intell. Robots Syst.*, pages 1970–1975, 2012.
- [45] K. Sreenath, H.-W. Park, I. Poulakakis, and J. Grizzle. A compliant hybrid zero dynamics controller for stable, efficient and fast bipedal walking on MABEL. *Int. J. Robot. Res.*, 30(9):1170–1193, 2011.
- [46] K. Sreenath, H.-W. Park, I. Poulakakis, and J. Grizzle. Embedding active force control within the compliant hybrid zero dynamics to achieve stable, fast running on MABEL. *Int. J. Robot. Res.*, 32(3):324–345, 2013.

- [47] R. Van Ham, T. G. Sugar, B. Vanderborght, K. W. Hollander, and D. Lefeber. Compliant actuator designs. *IEEE Robot. Autom. Mag.*, 16(3):81–94, Sep. 2009.
- [48] S. Veer and S. Sujatha. Approximate spring balancing of linkages to reduce actuator requirements. *Mechanism and Machine Theory*, 86:108 – 124, 2015.
- [49] T. Yang, E.R. Westervelt, J. P. Schmiedeler, and R.A. Bockbrader. Design and control of a planar bipedal robot ERNIE with parallel knee compliance. *Auton. Robots*, 25(4):317–330, 2008.
- [50] Y. Yesilevskiy, Z. Gan, and C.D. Remy. Optimal configuration of series and parallel elasticity in a 2D monopod. In *Proc. IEEE Int. Conf. Robot. Autom.*, pages 1360–1365, 2016.

Appendix
COPYRIGHT PERMISSIONS

This thesis includes materials reused from papers including [\[26\]](#), and [\[27\]](#). The reuse permissions from IEEE are attached in the following pages.



Title: SPEAR: A monopedal robot with Switchable Parallel Elastic actuation

Conference Proceedings: 2015 IEEE/RSJ International Conference on Intelligent Robots and Systems (IROS)

Author: Xin Liu

Publisher: IEEE

Date: September 2015

Copyright © 2015, IEEE

LOGIN

If you're a [copyright.com user](#), you can login to RightsLink using your copyright.com credentials. Already a [RightsLink user](#) or want to [learn more?](#)

Thesis / Dissertation Reuse

The IEEE does not require individuals working on a thesis to obtain a formal reuse license, however, you may print out this statement to be used as a permission grant:

Requirements to be followed when using any portion (e.g., figure, graph, table, or textual material) of an IEEE copyrighted paper in a thesis:

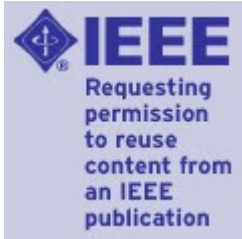
- 1) In the case of textual material (e.g., using short quotes or referring to the work within these papers) users must give full credit to the original source (author, paper, publication) followed by the IEEE copyright line © 2011 IEEE.
- 2) In the case of illustrations or tabular material, we require that the copyright line © [Year of original publication] IEEE appear prominently with each reprinted figure and/or table.
- 3) If a substantial portion of the original paper is to be used, and if you are not the senior author, also obtain the senior author's approval.

Requirements to be followed when using an entire IEEE copyrighted paper in a thesis:

- 1) The following IEEE copyright/ credit notice should be placed prominently in the references: © [year of original publication] IEEE. Reprinted, with permission, from [author names, paper title, IEEE publication title, and month/year of publication]
- 2) Only the accepted version of an IEEE copyrighted paper can be used when posting the paper or your thesis on-line.
- 3) In placing the thesis on the author's university website, please display the following message in a prominent place on the website: In reference to IEEE copyrighted material which is used with permission in this thesis, the IEEE does not endorse any of [university/educational entity's name goes here]'s products or services. Internal or personal use of this material is permitted. If interested in reprinting/republishing IEEE copyrighted material for advertising or promotional purposes or for creating new collective works for resale or redistribution, please go to http://www.ieee.org/publications_standards/publications/rights/rights_link.html to learn how to obtain a License from RightsLink.

If applicable, University Microfilms and/or ProQuest Library, or the Archives of Canada may supply single copies of the dissertation.

BACK**CLOSE WINDOW**



Title: A Switchable Parallel Elastic Actuator and its Application to Leg Design for Running Robots
Author: Xin Liu
Publication: Mechatronics, IEEE/ASME Transactions on
Publisher: IEEE
Date: Dec. 2018

Copyright © 2018, IEEE

LOGIN

If you're a [copyright.com user](#), you can login to RightsLink using your copyright.com credentials.

Already a [RightsLink user](#) or want to [learn more?](#)

Thesis / Dissertation Reuse

The IEEE does not require individuals working on a thesis to obtain a formal reuse license, however, you may print out this statement to be used as a permission grant:

Requirements to be followed when using any portion (e.g., figure, graph, table, or textual material) of an IEEE copyrighted paper in a thesis:

- 1) In the case of textual material (e.g., using short quotes or referring to the work within these papers) users must give full credit to the original source (author, paper, publication) followed by the IEEE copyright line © 2011 IEEE.
- 2) In the case of illustrations or tabular material, we require that the copyright line © [Year of original publication] IEEE appear prominently with each reprinted figure and/or table.
- 3) If a substantial portion of the original paper is to be used, and if you are not the senior author, also obtain the senior author's approval.

Requirements to be followed when using an entire IEEE copyrighted paper in a thesis:

- 1) The following IEEE copyright/ credit notice should be placed prominently in the references: © [year of original publication] IEEE. Reprinted, with permission, from [author names, paper title, IEEE publication title, and month/year of publication]
- 2) Only the accepted version of an IEEE copyrighted paper can be used when posting the paper or your thesis on-line.
- 3) In placing the thesis on the author's university website, please display the following message in a prominent place on the website: In reference to IEEE copyrighted material which is used with permission in this thesis, the IEEE does not endorse any of [university/educational entity's name goes here]'s products or services. Internal or personal use of this material is permitted. If interested in reprinting/republishing IEEE copyrighted material for advertising or promotional purposes or for creating new collective works for resale or redistribution, please go to http://www.ieee.org/publications_standards/publications/rights/rights_link.html to learn how to obtain a License from RightsLink.

If applicable, University Microfilms and/or ProQuest Library, or the Archives of Canada may supply single copies of the dissertation.

BACK**CLOSE WINDOW**